ELSEVIER

Contents lists available at ScienceDirect

Deep-Sea Research Part II

journal homepage: www.elsevier.com/locate/dsr2





Impact of the Gulf Stream on ocean waves

Mohammad Nabi Allahdadi a,*, Ruoying Hea, Vincent S. Neary

- Department of Marine, Earth, and Atmospheric Sciences, North Carolina State University, Raleigh, NC, 27695, USA
- Water Power Technologies, Sandia National Laboratories, Albuquerque, NM, 87185, USA

ARTICLE INFO

Keyword:
Modulation of waves by currents
Wave reflection
Wave straining
Wave momentum flux
Wave energy

ABSTRACT

Surface wave propagation and the modulations of wave parametric and spectral properties over the Gulf Stream (GS) are studied using a high spatial resolution (1 km) wave model that considers an idealized GS. While simulation results are generally consistent with a previous modelling study, we found that for following-current (FC) cases, reflection from the GS substantially increases wave height on the offshore side of the GS center by up to 25%, and decreases wave height on the landward side of the GS by as much as 80%. In the counter-current (CC) cases, the wave height profile is more symmetrical relative to the GS centerline, and the maximum 33% increase of wave height is predominantly driven by straining. The GS also causes an increase (decrease) in wavelength and directional spreading in the FC (CC) case. Additional model sensitivity experiments that further consider realistic shelf-ocean topography show that current modulation and bottom dissipation work in concert as low- and high-pass filters on the wave frequency spectra. Wave parameters and spectral modulations imposed by the GS have significant impacts on ocean-atmosphere momentum flux and wave energy resource.

1. Introduction

Modulation of wave characteristics by currents is an important ocean process that has drawn the attention of the marine science research community for decades (e.g. McKee, 1975; Tolman, 1990; Holthuijsen and Tolman, 1991; Tamura et al., 2008; Moreira and Peregrine, 2012; Barnes and Rautenbach, 2020). Earlier studies have shown that a strong ambient current can change wave parameters including wave height, length, direction, and directional spreading. The oceanic and coastal wave climate can thus be altered significantly due to strong wave-current interactions or modulation of waves by currents during both storm and normal conditions (Romero et al., 2017; Hegermiller et al., 2019). Moreover, rogue waves, one of the most energetic ocean phenomena, are usually generated as a result of amplification of wave height by opposing currents (Onorato et al., 2013). They are a dangerous marine hazard to ocean transportation and are frequently observed over western boundary currents (WBCs) including the Agulhas and Gulf Stream (Toffoli et al., 2015; Barnes and Rautenbach, 2020). Recently, mesoscale and sub-mesoscale currents in the form of eddies, fronts, and filaments have also been identified as major sources of significant small-scale wave height variability (e.g. Ardhuin et al., 2017). Modulation of waves by currents also play a major role in altering marine boundary layer dynamics, leading to large variations in momentum,

heat, and moisture flux transfers between ocean and atmosphere (e.g. Chalikov and Rainchik, 2011; Chalikov, 2018; Chalikov and Babanin, 2019).

Ocean currents have specific impacts on wave propagation and transformation. These include wave refraction, straining (deep-water shoaling due to current impact), trapping, reflection, and changes in the spectral shapes of the incident waves. Refraction of surface waves by currents was initially addressed by Johnson (1947). Tolman (1990) and Bascheck (2005) subsequently derived analytical equations for calculating the wave amplitude change due to straining over currents. Analysis of other complicated effects including wave reflection from a current and wave trapping inside a current are done by direct solution of the equations of motion using perturbation or alternative analytical methods (Peregrine, 1976; Liu et al., 1992; Shyu and Tung, 1999). Numerical wave models in both idealized and realistic settings were also employed to study the effects of currents on wave modulation (e.g. Holthuijsen and Tolman, 1991; Rusu et al., 2011; Hopkins et al., 2016; Barnes and Rautenbach, 2020; Prakash and Pant, 2020; Ponce de León and Soares, 2021; Lavaud et al., 2020; Beya et al., 2021).

One of the most intriguing processes is how waves respond to strong WBCs such as the Gulf Stream (GS). The GS is a persistent and intense current with a maximum surface velocity of 1.5–2.0 m s⁻¹ (e.g. Misra, 2020; Zeng and He, 2016) and a width of 100–300 km depending on

^{*} Corresponding author. 2800 Faucette Drive, Raleigh, NC, 27695, USA. E-mail address: mallahd@ncsu.edu (M.N. Allahdadi).

latitude (Gangopadhyay et al., 2016). Many observations of the G8 impact on waves propagating from outside the current have been documented (e.g. Meadows et al., 1983; Dobson and Irvine, 1983; McLeish and Ross, 1985; Liu et al., 1989). Compared to the regions outside the current, more complicated wave patterns and larger wave heights have been known to occur inside the GS. Furthermore, near-shore/coastal wave characteristics can be significantly modulated by the GS. To examine this modulation, we used in situ wave measurements at NDBC stations 41002 and 41013, which are located on the offshore and coastal sides of the GS, respectively (Fig. 1).

Measurements show many occasions when offshore wave height and direction were substantially altered by the GS. For the specific time we examined (the solid vertical line in Fig. 1b), the offshore wave approached the GS from the south with a mean angle of 20° with respect to the GS flow direction (i.e. a following-current case). Wind speed at this time was close to zero at the offshore station; therefore, no significant wave generation by wind was expected between the offshore buoy and the eastern edge of the GS.

We estimated that it would take approximately 8 h for waves to propagate from the offshore buoy to the coastal buoy. The time lag between two buoys was calculated based on the distance between two buoys, the average wave period measured at 41002, and wave celerity calculated using the wave dispersion equation. Wave spectra were computed and compared in Fig. 1c and d with the analysis on the coastal buoy performed on data collected 8 h later than that of the offshore buoy. Substantial decreases in the spectral energy and counterclockwise rotation of the main energy band was observed in the 2D spectra (Fig. 1c and d). At the coastal buoy, deep water conditions were satisfied; therefore, the changes in wave energy and direction cannot be attributed to depth-induced refraction. The 2D energy spectrum at the coastal buoy shows two major sectors. The energy in the southern sector (red circle in Fig. 1c) resulted from the alteration of offshore waves by the GS, whereas energy in the northeastern sector was largely the result of waves locally generated by the northerly-northeasterly winds (up to 8 m s⁻¹ based on measurements at NDBC41013) on the coastal side.

Numerical simulations have been used to address the effect of the GS on both swell propagation and wind-wave generation (e.g. Tolman, 1990; Holthuijsen and Tolman, 1991; Ponce de León and Soares, 2021). The study of Holthuijsen and Tolman (1991; hereafter referred to as HT91) offers many insightful analyses about the variations of wave

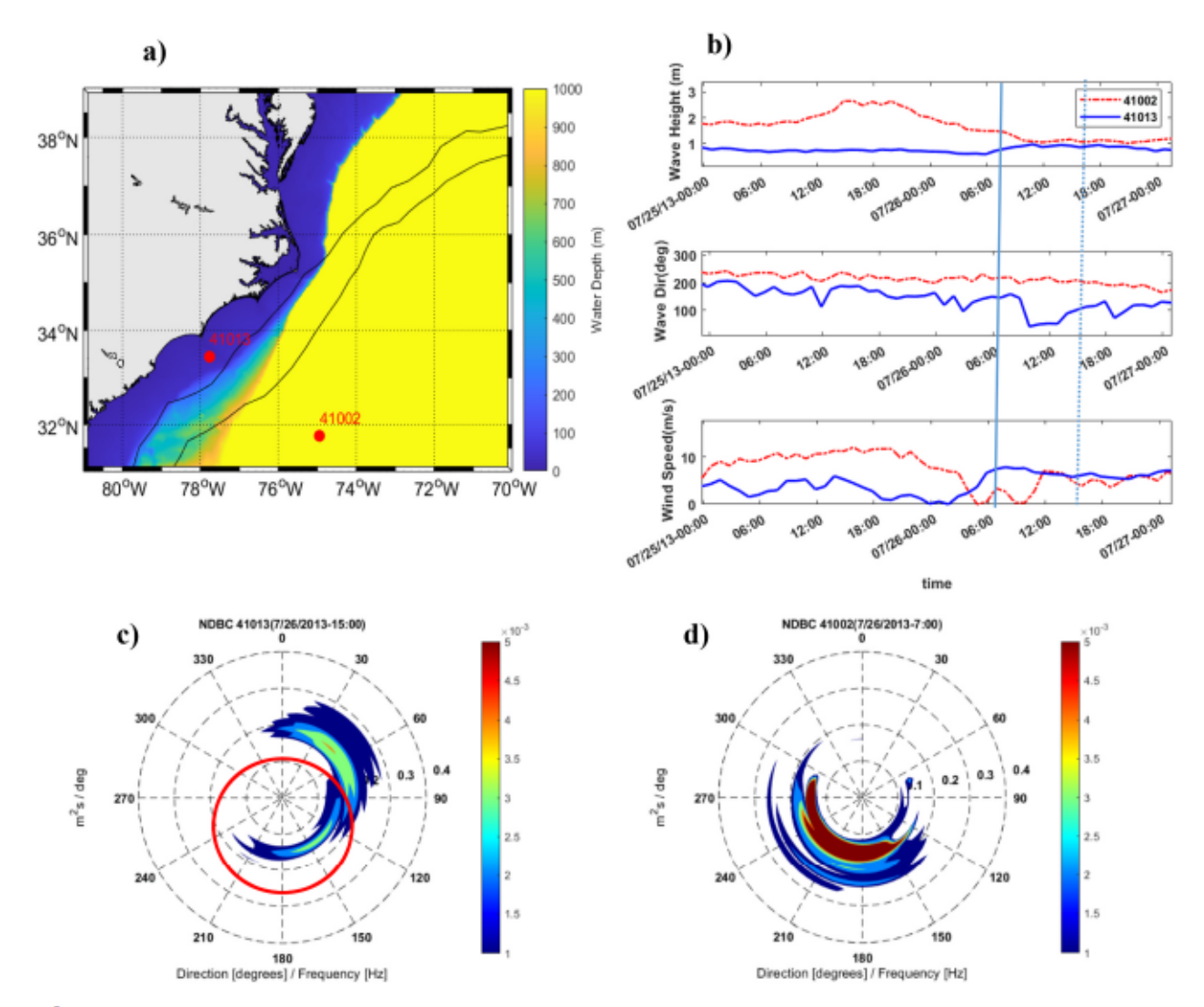


Fig. 1. a) Locations of two NDBC buoys on the offshore and coastal sides of the GS used for examining the effect of GS on offshore waves. The color-coded contours show the bathymetry of the region. The solid black lines show the average location of the GS boundaries based on NOAA data. b) Timeseries of measured wave height and direction at offshore and coastal buoys and measured 10-m wind at speed at the offshore buoy 41002. The vertical solid line specifies the time corresponding to near-zero wind speed at NDBC 41002 for which the offshore spectrum is presented. The solid (dashed) line is corresponding to the time for which the wave spectrum at the offshore buoy NDBC 41002 (coastal buoy NDBC 41013) is presented; c,d) measured 2D spectra at the coastal and offshore buoy respectively corresponding to the specified times in panel b. The 8 h' time lag is to account for the approximate time it requires for the waves to propagate from NDBC 41002 to NDBC 41013. The red circle in (c) shows the part of the spectral energy propagated from the offshore and modulated by the GS.

parameters due to the impacts of currents. They used a third-generation wave model that implemented an idealized GS and GS ring. For the case of an idealized, straight GS, they considered both swell propagation across the GS and active wave generation by the wind for both following-current (FC) and counter-current (CC) cases, which are defined by the incident wave or wind direction relative to the G8 (see Appendix A for definitions of FC and CC). For swells crossing the GS, they used a quasi-1D model with a spatial resolution of 14 km for which all the lateral gradients contributing to the spatial energy propagation were set to zero. This idealization assumed that the GS is infinitely long. They also used a Gaussian distribution of surface current speeds across a 150 km transverse with a maximum current speed of 1.7 m s⁻¹ in the middle of the GS. For the FC case, their simulation showed that the directional spectra on the east of the GS are modulated by wave reflection from the GS, whereas no reflection was detected on the west side. Therefore, wave height slightly increased in the eastern region of the GS, while the original wave height for the rest of the cross-section was unchanged. For the CC case, their model analyses showed that for a specific wave direction and peak period, the negative and positive mechanisms contributing to changing wave height almost canceled out in the middle of the GS and no significant change of the wave height resulted. The HT91 study also touched upon the mechanisms affecting swells crossing the GS and is one of the first studies quantifying swell wave variations across the GS.

The goal of this study is to revisit the seminal work of HT91 by using an advanced spectral wave model with a much higher (1 km as opposed to 14 km) spatial resolution. This high spatial resolution is essential to resolve high velocity gradients across an idealized GS. Compared to the 1D simulation of HT91, the present study used a fully 2D model in the spatial domain. This 2D model is more realistic and accurate than the 1D model, especially when simulating the following-current waves for which the reflected waves from the upstream regions add up to the waves in the offshore regions of the downstream regions. Also, the wave field on the coastal (west) side of the GS will be simulated more

accurately since the lateral wave energy can be correctly transferred to the interested areas. New analyses built on the high-resolution model simulations herein present a more detailed assessment of ocean current impacts on wave modulation. These analyses include extensive investigations on incident waves coming from different directions, quantification of mechanisms contributing to modulating wave properties, and examination of wave spectral variations induced by the GS current. The novel implications of these parametric and spectral modulations for ocean-atmosphere coupling and wave energy characterization are also discussed herein. For the sake of brevity, technical details and term definitions are presented in Appendix A.

2. Numerical model specifications

2.1. Numerical model

We used the third-generation wave model Simulating WAves Nearshore (SWAN, 2015) on an unstructured mesh (Zijlema, 2009, 2010) in an idealized setting to study the GS's effect on waves. Instead of using a quasi-1D model setup with zero lateral gradients as HT91 did, we used a fully 2D model configuration with propagation along both x- and y-axes. This is more realistic and accurate, especially for the FC cases for which the reflected waves from upstream locations are combined with the incoming waves at downstream offshore locations (see Fig. 2b and Appendix A for definitions of FC, CC, upstream, and downstream). These reflected waves need to be included to achieve more accurate results on the eastern regions of the GS. Furthermore, on the downwave side of the GS, coastal wave characteristics can be affected by waves crossing the GS from downstream locations. The equation for the conservation of wave action density is modified as follows to include background current effects (Zijlema, 2009, 2010; SWAN, 2015):

$$\frac{\partial N}{\partial t} + \nabla_{\overrightarrow{x}} \cdot \left[\left(\overrightarrow{c}_g + \overrightarrow{U} \right) N \right] + \frac{\partial c_\sigma N}{\partial \sigma} + \frac{\partial c_\theta N}{\partial \theta} = \frac{S_{tot}}{\sigma}$$
(1)

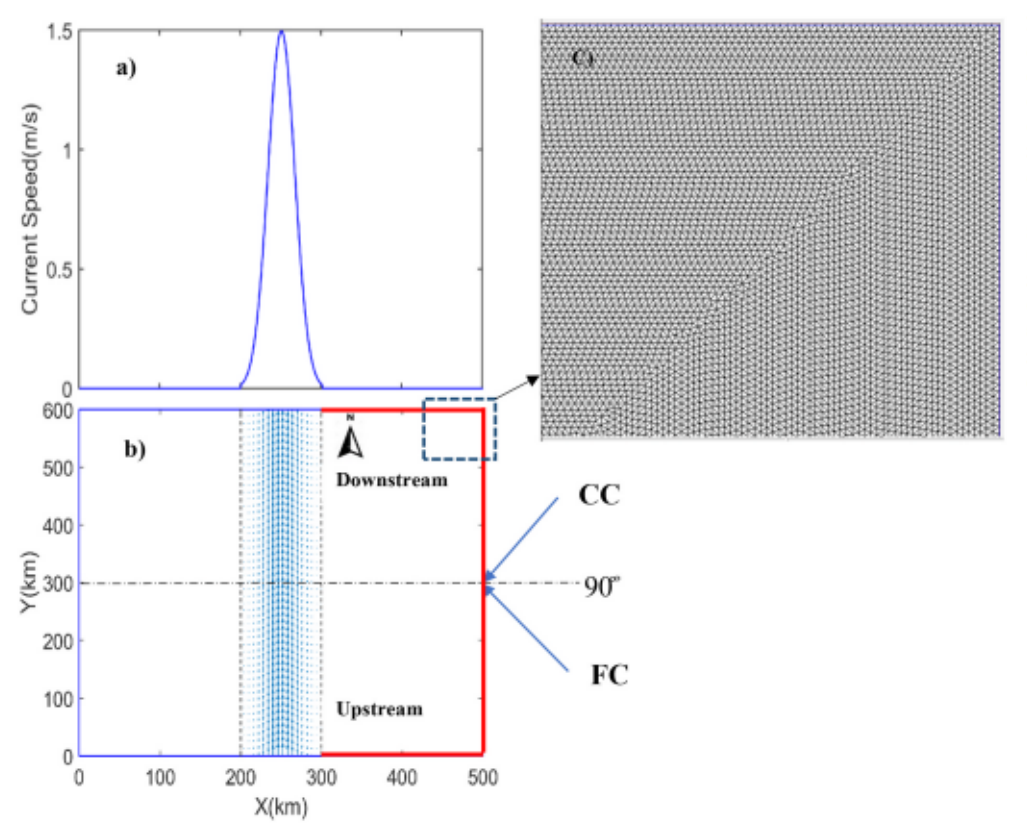


Fig. 2. a) Distribution of current speed across the GS and modeling area. b) Model extent in x and y directions and the location of the GS. The vectors show the south-north current vector with maximum speed of 1.5 ms-1 in the center. The model. The arrows on at the eastern model open boundary (at X = 500 km) next to the 90° line show the general direction of the following-current (FC) and counter-current(CC) waves with respect to the direction perpendicular to the current (90° line). Open boundaries are specified with red lines in Fig. 2b and c) the model computational mesh for the specified dashed box shown in panel (b).

where N is the wave action density, t is time, c_g is wave group velocity vector, U is the current vector, x is the spatial vector that includes x and y components, and S_{tot} is the sum of source terms. The effect of currents on wave action is quantified through the four terms on the left-hand side in Eq. (1). The second term from the left quantifies the spatial variations of wave energy propagation. The propagation speed here is the sum of the group velocity of the wave (in a frame of reference moving with the current) and current speed. This term accounts for the effects of shoaling (depth-induced wave amplification) and straining (current-induced wave amplification):

The third term from the left in Eq. (1) includes the effect of the shift in radian frequency on wave action. The rate of change for radiant frequency (c) is a function of depth and current variations in time and space:

$$(3)$$

The effect of depth- and current-induced refraction on wave action is included in the fourth term from the left in Eq. (1) through the parameter c:

In the above equations, k is the wavenumber vector, d is water depth, is the wave radian frequency, is the direction of wave spectral component, s is the axis parallel to the direction of wave propagation, and m is the axis perpendicular to the propagation direction. The effect of currents on wave action can also be included in the source term S_{tot} on the right side of Eq. (1) by modifying the relative wind speed used in the calculation of wind stress in the wind input source term. Since in the present modeling no generation by wind is considered, the related source term is zero.

2.2. Model design

For our idealized model setup, the GS was approximated by a Gaussian current jet 600 km long and 100 km wide. This is a good representative of the average GS width, especially south of Cape Hatteras, North Carolina, USA (e.g. Gangopadhyay et al., 2016). This Gaussian distribution had a maximum current speed 1.5 m s⁻¹ at the middle, which is close to the maximum speed of 1.7 m s⁻¹ used in HT91 (Fig. 2a). For expediency, hypothetical GS flow was south to north and all incident wave directions (IWD) were evaluated relative to this. To assure that simulation results were not adversely affected by boundaries, the model dimension in the x direction was determined based on a sensitivity analysis of different model widths (300 800 km). In sensitivity analysis for the modeling area, we considered two goals: 1. minimizing the effect of offshore boundary on the incident waves by providing a buffer zone that is not affected by the reflected waves from the GS, so larger distances between the right border of the GS and the eastern boundary were intended (it was concluded that 300 km is not large enough); 2. optimizing the simulation time/cost by avoiding unnecessary large distances between the right border of the GS and the eastern boundary (it was concluded that 800 km doesn t add much to model accuracy, but significantly increase the simulation time). The x-axis dimension of 500 km was the optimum fulfilling both condition. As a result, we adopted a 500 km 600 km rectangular modeling area. The ocean region on the coastal and offshore sides of the GS were each 250 km wide. (Fig. 2b). Swells enter the model from the east (right) side of the model at x 500 km (Fig. 2b) to the left. Also, parts of the model northern and southern boundaries on the east side of the GS are considered as the open boundary and waves can propagate through these parts (the open boundaries are specified with red lines in Fig. 2b).

Our model simulations used a spatial resolution of 1 km. This is much higher than the model resolution of HT91, which was 14 km (only 10 $\,11$ computational grids across their hypothetical GS). The 1 km resolution adopted in this study allows our simulations to resolve well the GS s velocity gradient and the current-induced wave variations. The Control model simulation used a constant water depth of 500 m. We also experimented with model bathymetry that mimics the coastal bathymetry and shelf break in a model sensitivity run (Section 4) to investigate the effect of water depth on modulation of waves by currents over the GS.

2.2.1. Model setup and experiments

The simulations herein included only swells propagating over the GS, without any active wave generation by the wind. A similar model experiment design to that of HT91 was used (Table 1). Incident swells were applied to the model through the open boundaries on three sides (the western boundary was masked as land). Various configurations of open ocean waves were applied at the eastern boundary and/or the offshore side (eastern side) of the GS along the northern and southern boundaries. No wave was applied on the coastal side or over the GS so that we could focus on the open ocean waves and how they are modulated by the GS before propagating to the coastal zone. Swells at the open boundaries were introduced by their bulk parameters including wave height, peak period, direction, and directional spreading; thus the frequency-directional spectrum across the GS can be calculated using the spectral model applied on the spectral boundary conditions. These parameters were used for establishing a wave frequency-direction spectrum. Variations of swell energy with frequency can be appropriately represented by either single-peaked distributions, Gaussian, or JONSWAP (Hasselmann et al., 1973). HT91 used a Gaussian distribution, but in the present paper, we chose the JONSWAP spectrum for input waves because it is more accurate, especially for younger swells in which energy in the higher frequency ranges is dominant (Lucas and Guedes Soares, 2015). A standard directional distribution of peak was used, for which is the direction of each energy component and $_{peak}$ is the peak wave direction. Consistent with HT91, a typical value of 12.4 was used as the directional spreading of the incident waves, which corresponds to m 20 and accounts for a very narrow directional distribution. Similar to HT91, incident wave height (H_s) of 1.99 m and peak frequency (f_p) of 0.071 Hz (peak period of 14.08 s) were used for this simulation. The frequency-domain for model simulation was 0.04 0.15 Hz, which is almost the same as HT91. An optimum number of frequencies (nf) of 36 for the discretization of this

Table 1Summary of the input wave characteristics and numerical parameters used in the simulations.

Characteristic	Symbol (unit)	value
Boundary condition		
Significant wave height	H_s m	1.99
Frequency spectrum		JONSWAP
Peak frequency	f_p Hz	0.071
Peak parameter	•	3.3
Dimensionless spectral width	$af f_p$	0.07
	$_{b}f$ f_{p}	0.09
Directional spreading	DSPR(degrees)	12.4
- Numerical model parameters		
Spatial resolution	ds (m)	1000
Timestep	t (min)	10
Number of frequencies	nf	36
Minimum frequency	fmin Hz	0.04
Maximum frequency	fmax Hz	0.15
Number of spectral directions	nd	48

domain was obtained by a sensitivity analysis of different nf values in the range of 24 72 as advised by Allahdadi et al. (2019a). Two general categories of simulation cases, following-current (FC) and counter-current (CC), were examined in the model analyses. Based on the south-to-north flow of the idealized GS in this study, FC directions included incident waves from 90 to 180 relative to model north while the CC cases included directions between 0 and 90. Following HT91, the initial number of spectral directions (nd) was 48, resulting in 7.5 directional sectors for both FC and CC cases. Neu and Won (1990), and later HT91, reported that for a narrow spectral distribution similar to the one assumed for swells, if the directional resolution is not small enough, the incident wave energy from the CC directions (0 90) bifurcates in the direction of the GS because of the spurious energy diffusion caused by lack of spectral directional resolution. Model test simulations using directional resolutions between 10 and 2.5 for several IWDs and examination of the frequency-direction spectra for the CC cases showed that bifurcation resulted for all values of directional resolution, but the amount of the bifurcated energy was significantly decreased as directional resolution increased. In the calculation of wave parameters for these directions, this spurious energy was filtered out and all parameters were calculated based on the corrected spectra. The filtering procedure was consistent with the approach done in HT91, and it effectively removed the spurious energy produced either in or near the direction of the GS from the frequency-directional spectra.

3. Results

3.1. Analytical solutions

Equations (1) (4) in section 2.1 describe the wave dynamics that include the effect of currents. Due to their complexity, these equations need to be solved numerically. However, for cases considering constant water depth and spatially uniform ambient current, the governing equations for wave crest rotation and wave height amplification can be simplified and solved analytically. Their solutions can subsequently be used as a reference for a general examination of the current-induced modulation of wave parameters derived from numerical model simulations.

By considering the continuity of wave crests over the current region and outside the current, Johnson (1947) derived a simple equation to predict the changes in wave direction due to refraction caused by the current:

where $_1$ is the angle between the IWD and current, $_2$ is the angle between the wave direction over the current and current direction, and C_1 is the wave celerity before it propagates over the current. Based on the former studies such as HT91 and its references, analytical equations were also derived for wave height amplification over the current due to mechanisms including refraction, radiation stress work, and straining:

$$(7)$$

where a_2 and a_1 are wave amplitudes over the current and outside the current region, respectively; k_2 and k_1 are corresponding wavenumbers; U_p is the current speed in the direction of wave propagation; and C_g is the wave group velocity in a frame of reference moving with the current.

Wave amplification due to refraction (Eq. (6)) is derived by assuming conservation of wave energy flux between two specific wave rays (Dean and Dalrymple, 1991). The amplification due to radiation stress (Eq. (7)) is the work done due to a change in wavelength, which is translated as the wave number. Amplification of wave height due to straining (Eq. (8)) is the equivalent of shoaling induced by depth variations, except here it was induced by currents. The amount of wave height amplification due to these three mechanisms is a function of wave period (frequency) and the intensity of the ambient current.

Analytical solutions have also been derived for the modulation of frequency spectra by currents. Hedges (1980) used the principle of wave action conservation presented by Bretherton et al. (1968) and derived an equation to estimate the frequency spectrum of swells altered by currents (S_r versus the spectrum over a quiescent region (S_a :

where $_r$ is the angular frequency of each spectral component in the quiescent region and g is acceleration due to gravity. The angular frequency over the current ($_a$ is calculated as a function of $_r$, wave number k, current speed U and the angle between the current and wave orthogonal:

(10)

In the derivation of Eq. (9), variations of wave direction and wavenumber (refraction and radiation stress work) due to currents were not included, so changes in the spectral energy are attributed to straining.

Although Equations (5) (8) were primarily derived for monochromatic waves, to better understand the intensity of each mechanism within the normal spectral frequency range of U.S. East Coast waves (0.04 0.6 Hz, as specified by Allahdadi et al., 2019b), variations of these amplification factors were calculated and plotted across the 100 km-wide GS filament used for our simulations (Fig. 3). The results are shown for IWDs of 45 (CC) and 135 (FC). The x-axis for this model domain includes the 100 km-wide GS (western and eastern boundaries of the GS are at x 200 km and x 300 km respectively), plus 50 km on each side of the GS. Starting from the eastern boundary of the GS, current speed and wave parameters were fed into Equations (5) (9) to calculate the effect of the current on wave parameters at each location across the GS. Calculations were carried out for the entire width of the GS and for different peak frequencies (periods) of the incident waves. Calculated amplification factors due to refraction, straining, and radiation stress work across the GS (x-axis) and versus different incident wave frequencies (y-axis) were compared for both FC (incidence angle 135) and CC (incidence angle 45) waves(Fig. 3). Note that calculations were only across the GS (200 x 300 km). For the area outside of the GS where current speeds 0, including the eastern and western GS borders, values from the very east and west edges of the GS were extended to these regions.

In general, for the FC case, only refraction increased the wave amplitude, and both straining and radiation stress work caused amplitude reduction (Fig. 3a c). The amplification factor due to refraction increased as it approached the center of the GS and increased the wave frequency to about 0.45 Hz. For higher frequencies near the intense current in the center of the GS, the corresponding short waves were intensely refracted back from the center, thereby decreasing amplification. Both straining and radiation stresses reduced wave height in the FC case (amplification factors 1) for all frequencies across the GS, with maximum reductions corresponding to the center of the GS and highest frequencies. For the CC case, calculations show the opposite behavior for all three mechanisms compared to those of the FC case. Refraction turns the wave direction more orthogonal to currents, causing divergence in the energy propagation that is translated as smaller amplification factors over the current (HT91). It therefore causes amplification factors 1 for all frequencies across the GS (Fig. 3d). Like depth-induced wave

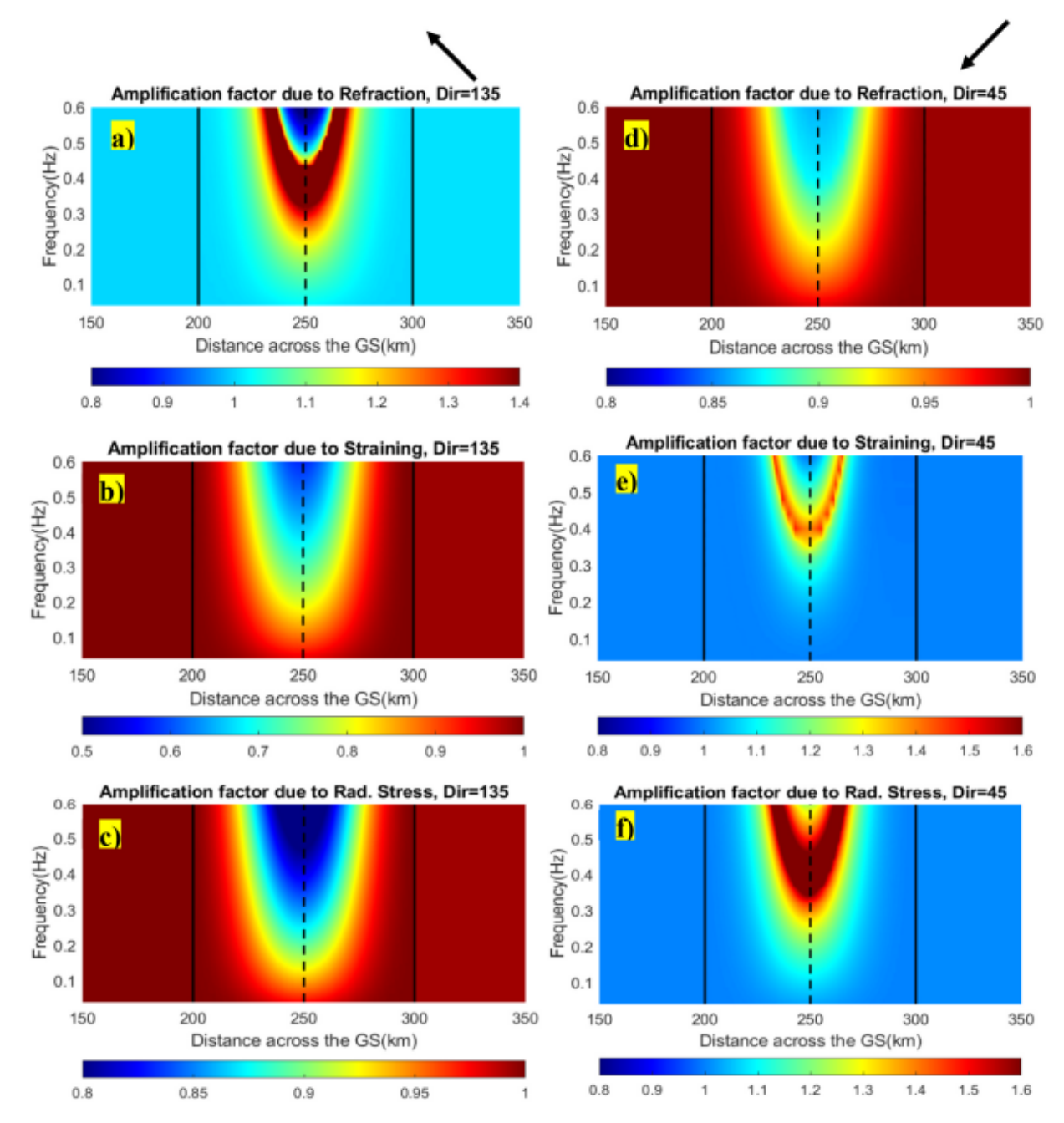


Fig. 3. Variations of wave height amplification factors (color shading) predicted by analytical models due to different mechanisms of modulation of waves by currents across the GS as a function of wave frequency. a-c) FC case: respectively, refraction, straining, and radiation stress work amplification factors. d-f) CC case: respectively, refraction, straining, and radiation stress work amplification factors. The eastern border, centerline, and western border of the GS correspond to 350, 250, and 200 km, respectively. This coordinate system is consistent with the model design in Fig. 2b. Please note the differences between color bars in different panels that are used for the sake of clarity. The vectors on the top of each row show the direction of incident wave for each case.

shoaling in shallow water, the CC slows wave celerity, increases wave steepness, and results in shorter wavelengths that contribute to wave amplification due to straining and radiation stress work (Fig. 3e and f).

3.2. Numerical model solutions: wave parameters

In this section, numerical model simulation results for the effect of the GS on swells in a model with a constant water depth of 500 m are presented. This water depth is much larger than half the wavelength of the incident wave with peak frequency of 0.071 Hz (peak period of 14.08 s) used for the simulations, and therefore can be considered deepwater wave propagation. Hence, all changes in wave characteristics over and in the vicinity of the GS can be attributed to the current effect. As in the previous section, FC and CC incident waves were examined. The FC cases included directions of 120° , 135° , 150° , and 160° , while waves from 0° , 15° , 30° , 45° , and 60° comprised the CC cases. Note that waves are propagating from east to west. The coordinates of input waves in the model is the entire eastern boundary (x = 500 km). Also, parts of northern and southern boundaries are open boundaries. For all the results and figures in this paper, model outputs are presented for a 200 km segment of the model between x = 350 km (offshore of the GS) and x = 150 km (shoreward of the GS), with the GS located between x = 200 km and x = 300 km, consistent with the model design shown in Fig. 2b.

In the FC cases, wave height on the east of the GS and over the right

half of the GS increased, which was more pronounced as the initial wave direction increased and waves became more parallel to the G8 (Fig. 4a). The wave amplification factor based on analytical Eqs. (7)-(9) did not show this trend. At 135°, the calculated analytical amplitude across the GS (Fig. 4e) showed almost no change, while the simulation results at 135° (Fig. 4a) showed an increase of about 10% (0.1 m) over the GS. This inconsistency was mostly the result of wave reflection from the GS for FC waves (Peregrine, 1976; McKee, 1977). This effect will be discussed in more detail in the next sections. Depending on wave direction, the increase in wave height stops somewhere between the middle and the eastern edge of the GS. For the largest examined wave direction (160°), wave height increased 25% (0.5 m) compared to the incident wave height of 1.99 m and occurred about 20 km from the eastern border of the GS. The value of the maximum wave height decreased, and the location shifted to the west as the incident wave became more oblique to the GS. Wave heights at the middle and west side of the GS decreased compared to incident wave height. This decrease was significant for larger wave directions. Over the western side of the GS, wave height decreased to 1.2 and 1.5 m for 150° and 160°, respectively. The

mitigating effect of the GS on wave height in the coastal area regarding the FC cases was as large as 80%. This decrease was the result of loss of wave energy to the GS and the partial reflection of wave energy to the right half of the GS (see section 3.3 for more details). While the results from HT91 for IWD of 135° showed slight increases and decreases on the east and west side of the GS, no detailed distinction of the wave reflection effect and decrease of wave height in coastal regions was discussed. Wave height changes for IWD of 135° (increase of 0.1 m over the GS and a decrease of 0.1 m in the coastal area; Fig. 4a)were not clearly detected by HT91, due to the much lower spatial resolution of the HT91 model smoothing smaller scale variations across the GS.

Contrary to the FC cases, wave height did not increase in the CC cases on the east side of the GS (Fig. 4b). Instead, the wave height profile over the GS was more symmetrical about the GS centerline. CC cases' wave height increases were consistent with the analytical results (see 45° in Fig. 4f). This implies that similar mechanisms for wave amplification of CC swells are included in the analytical results and the wave model. West of the GS, the wave height decrease was much smaller than in the FC cases. Wave height amplification over the GS, especially at the

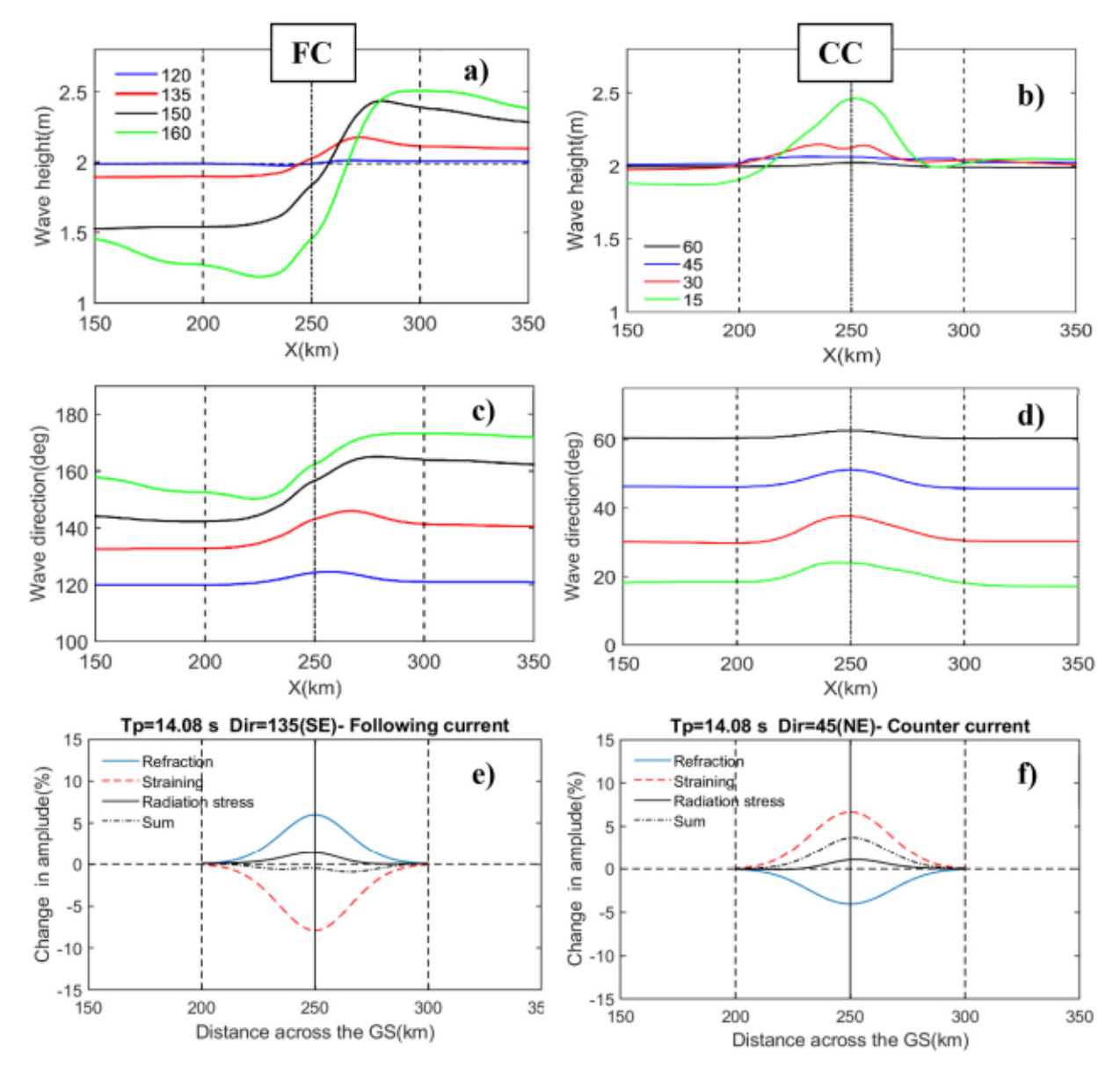


Fig. 4. a) and b) Variations of simulated wave height across the GS and the eastern and western regions for multiple FC and CC incident wave directions, respectively. Vertical dashed lines show GS western (200 km), center (250 km), and eastern (300 km) edges. c) and d) As for a) and b) but showing simulated wave directions. e) and f) Analytical wave amplification factors directly over the GS resulting from different mechanisms for FC and CC cases, respectively.

center, increased with decreasing incident wave angle (as waves oppose the GS current more). Wave height amplification for wave directions of 15° and 0° (not shown) was 22% (0.45 m) and 33% (0.65 m), respectively, above incident wave height. This significant increase of wave height over the current was mostly due to straining (Baschek, 2005; Barnes and Rautenbach, 2020).

Variations in wave direction for all FC cases showed a clockwise rotation over the eastern half of the GS that made the waves more parallel to the current (Fig. 4c). Waves started rotating counterclockwise toward the initial IWD to the west of the GS centerline, which was almost consistent with the location of maximum wave height across the model. A clockwise rotation that made the waves more orthogonal to currents was identified over the GS for all CC IWDs (Fig. 4d), due to refraction (also reported by HT91). The pattern of variations for

directional spreading (DSPR) across the GS for FS cases (not shown) was very similar to wave height, i.e. increasing over the eastern half of the GS and then decreasing as approaching the coastal region where DSPR was almost the same as incident wave DSPR (12.4°). For larger IWDs, DSPR increased up to 25°, which was twice the original DSPR. This increase of DSPR could have substantial implications for ocean-atmosphere boundary layer dynamics over the GS (Ting et al., 2012).

Wavelengths (not shown) also changed over the GS for both FC and CC cases as a result of straining and change of wave propagation speed induced by currents (not shown). For the FC (CC) cases, the out-of-GS wavelength of 310 m increased (decreased) over the GS and reached the maximum (minimum) at the center of the GS. The maximum FC wavelength increased with increasing wave direction and reached 350 m for an IWD of 160° (variations are not shown here for the sake of

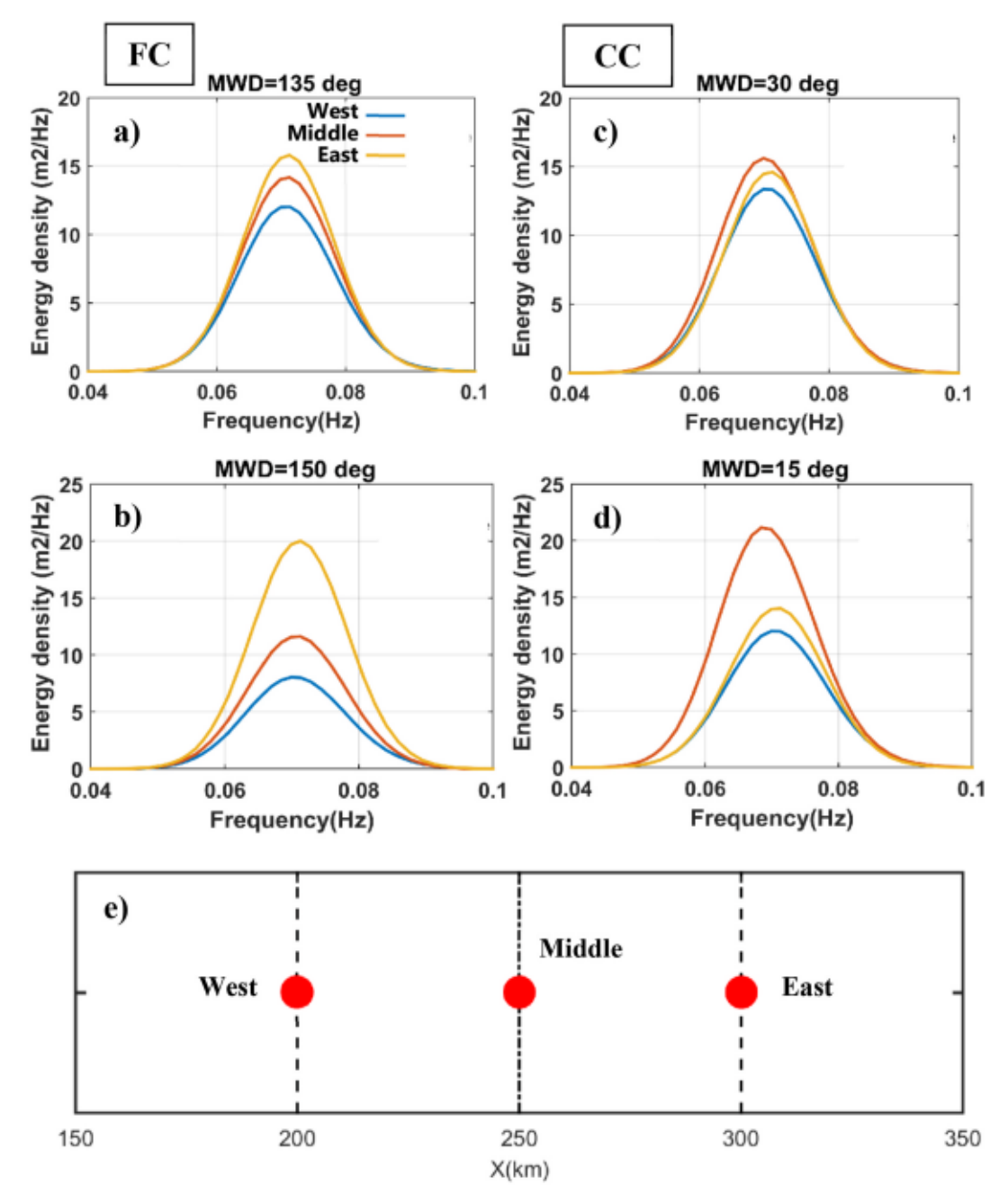


Fig. 5. Simulated frequency spectra at three locations across the GS for FC IWDs of a) 135° , b) 150° , and CC IWDs of c) 30° , and d) 15° . The extraction locations correspond to the GS's west edge (x = 200 km), middle (x = 250 km), and east edge (x = 300 km). MWD in the figure titles stands for Mean Wave Direction, which herein is the same as IWD. Please note that in panel (e), X = 500 and x = 0 km (not shown) represent the location of offshore and coast boundaries, respectively.

brevity). In the CC cases, wavelength decrease was more pronounced as IWD decreased and waves became more opposed to the current. For the IWD of 15°, wavelengths decreased to 280 m at the center of the GS.

3.3. Numerical model solutions: wave spectra

In addition to swell parameters, the spectral shape of an incident wave can also be altered by the GS. This includes the shape of the frequency spectra, peak frequency, and frequency-direction distribution of wave spectra, each of which has a specific implication in wave modeling and ocean-atmosphere boundary layer physics (Zieger et al., 2015; Chalikov and Babanin, 2019). As shown by Hedges (1980) and Eq. (9), for an ambient current with a component opposing the wave (the CC case with negative U), spectral energies at different frequencies (including peak energy) increase, while energy levels decrease for the FC case (positive U). Simulation results of frequency spectra for multiple CC and FC cases were consistent with this conclusion (Fig. 5). In the FC cases, spectral energy at all frequencies decreased at the middle (x = 250 km, see Fig. 5e for location) and western border (x = 200 km) of the GS compared to the energy on the east side. The decrease was more pronounced for IWDs more parallel to the current. In the FC cases, The spectral peak on the GS's eastern border (x = 300 km) was larger than the input spectrum due to the effect of wave reflection from the GS (Fig. 5a and b). The intact peak of spectral energy for the input spectrum with wave height of 1.99 m and the JONSWAP spectral shape was 14 m² Hz⁻¹. Similar to the analytical conclusion of Hedges (1980), spectral energies increased for the CC cases (Fig. 5c and d) with IWDs of 30° and 15°. The maximum enhancement of spectral energy for CC cases corresponded to the maximum current speed in the middle of the GS. The spectral peak on the east side of the GS was almost unchanged due to the

zero velocity of the opposing current at this location, while on the west side, the peak decreased compared to the input spectrum as a result of energy lost due to refraction.

In addition to the spectral energies, the spectral peak frequencies can be modified by currents (Eq. (10)). For simulated FC spectra in the middle of the GS, the spectral peak shifted to higher frequencies (4-6% higher than the original peak frequencies for the two directions shown in Fig. 5a and b), while for CC cases the spectral peaks in the middle of the GS shifted to lower frequencies (Fig. 5c and d). For the simulations presented herein (peak frequency of the incident wave = 0.071 Hz), the frequency spectra were almost symmetrical with respect to peak frequency, even after being altered by currents. However, simulation results for higher peak frequencies (0.1-0.15 Hz) showed that for FC cases, the current took more energy from the high-frequency lobe of the spectrum; that is, the GS acted like a low-pass filter.

The GS also altered the energy distribution within the frequency-directional space. Two-dimensional wave spectra of the CC waves became narrower directionally at the center of the GS, where their peaks of energy increased (as a result of straining) and the peak direction rotated clockwise (Fig. 6b). The spectral distribution on the west and east sides of the GS were very similar and consistent with the spectral distribution of the incident waves, although the energy peak for the spectrum on the west decreased (Fig. 6a,c). The additional spectral components indicated by the red ellipses for the CC case (Fig. 6a-c) are not real. They result from the spurious energy diffusion caused by the opposite current and are attributed to the discontinuity in solving directional model equations. Although these results were obtained from a very fine directional resolution (2.5°), some spurious energy diffusion was still observed. These unreal parts of the simulated spectra were filtered out in calculations of wave parameters in previous sections.

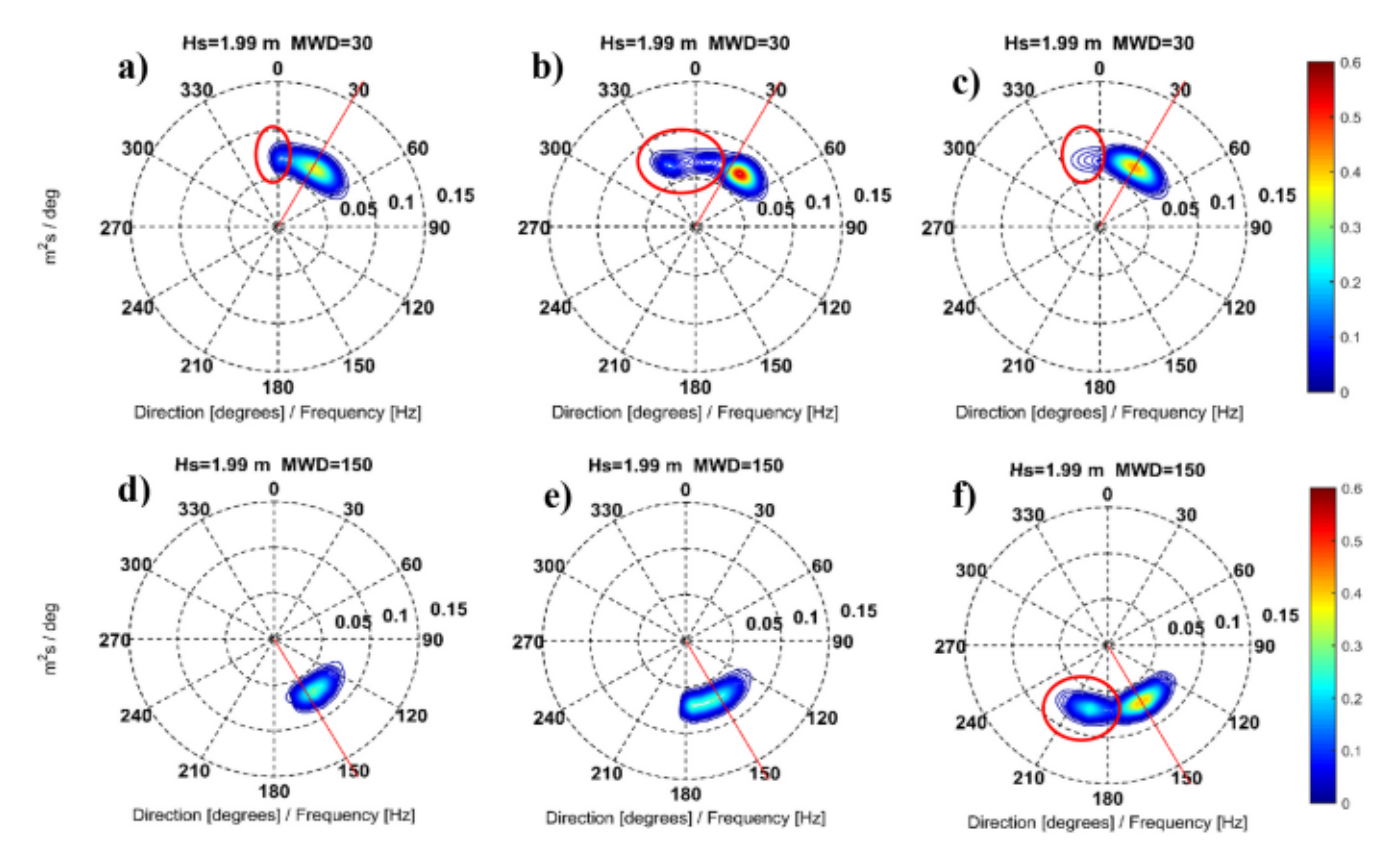


Fig. 6. Samples of simulated frequency-directional spectra across the GS for one CC IWD (30°) and one FC IWD (150°). a-c) Spectra for 30° at the GS western boundary (x = 200 km), middle (x = 250 km), and eastern boundary (x = 300 km), respectively. d-f) Same as for a-c but for IWD of 150°. Red ellipses in a-c specify the numerically diffused spectral components that are associated only with CC cases and were filtered out in the calculation of wave parameters. The red ellipse in (f) shows the spectral components reflected from the GS as a realistic response of FC cases to the GS. The red straight lines show the IWD. MWD in the figure titles stands for Mean Wave Direction which herein is the same as IWD.

Unlike the CC cases, the additional directional component in the frequency-direction spectra of FC cases on the east and over the GS were realistic (Fig. 6f) and were the result of wave reflection from the GS when the incident wave included a FC component (Peregrine, 1976). This reflected energy accounts for wave height amplification and increased wave directional spreading over the eastern half of the GS. In the middle of the GS, the spectrum included only one spectral peak and no reflected components were observed (Fig. 6e). The spectral peak there had a larger directional extension with a clockwise rotation relative to the IWD, making the spectral components more parallel to the current. On the western side of the GS, the spectral peak and directional spreading decreased, owing to dissipation by the current effect and loss of energy by reflection over the GS.

The spectral peak and the total energy east of the GS and its right half increased as incident FC waves became more parallel to the current (Fig. 5) due to increased energy reflected from the GS. Based on the theoretical studies of McKee (1975) and Peregrine (1976), reflection occurs when the current-induced refraction changes the wave direction to be near-parallel to the ambient current. This corresponds to the formation of caustics across the current. For monochromatic waves, they showed that the reflection coefficient varies from zero for IWD perpendicular to the current to 1 (total reflection) for waves completely parallel to the current. Not all the spectral components of the incident wave experience the same amount of refraction. Higher frequency components with larger directional deviations from the mean wave direction (MWD) of the spectrum (i.e. components more parallel to the current) are more prone to be refracted and potentially can be reflected (see Fig. 3a for frequency effect). Reflection coefficients for different FC IWDs were calculated by separating the directional spectral components corresponding to the reflected waves from the main spectral components. The reflection-associated wave heights were determined by integrating the reflection spectra in frequency and directional space. By dividing the resultant wave heights by the input wave heights, the reflection coefficients were obtained (Fig. 7a). East of the GS center, the maximum reflection coefficient increased from 0.05 for an IWD of 120° to 0.2 for an IWD of 160°. No reflection occurred west of the GS centerline (west of x = 250 km) due to the reverse refraction of the spectral components encountering decreasing current speed. This reverse refraction is a function of the first derivative of current with respect to distance (Eq. (4) and Fig. 7b).

4. Discussion

4.1. Variable depth

Simulation results in the previous section were for a constant-depth, deep-water wave for which the roughness of the seabed did not dissipate wave energy. The response of waves to currents is expected to be more complex with realistic shelf-break topography. Here, a model was set up with variable depths across the continental shelf and the GS. Model bathymetry, the location of the shelf break, and the average depth for the coastal area were idealized from available bathymetry data and location maps of the GS (Berline et al., 2006) for regions southeast of Cape Hatters, North Carolina (U.S.) (Fig. 8). Water depth in the coastal area (x = 0–150 km) was 50 m. The shelf break was located at x = 150 km, 50 km west of the GS. Water depth increased linearly from 50 m at the shelf break to 500 m at the east edge of the GS, then remained a constant 500 m in the offshore region. In SWAN, dissipation of wave energy due to bottom friction for each spectral component $B(\sigma,\theta)$ is quantified as:

$$S_{ds,b} = -C_b \frac{\sigma^2}{\sigma^2 \sin h^2 k d} E(\sigma, \theta) \qquad (11)$$

where C_b is a bottom friction coefficient and d is water depth. Following Hasselmann et al. (1973), a constant value of 0.038 m^2s^{-3} for C_b was used, representing a typical sandy bottom for the study region.

Simulation results from the models with constant depth and with variable depth for incoming waves with peak periods of 14.08 s or less (12, 11, and 10 s) showed no significant changes in the wave characteristics over the GS and its eastside (Fig. 9). On the west side of the GS, the effect of water depth on wave characteristics became significant close to the shelf-break where water depth = 50 m. Therefore, all changes in the wave profile over and in the vicinity of the GS were attributed to current effects discussed in previous sections.

This behavior can be understood based on the maximum wavelength corresponding to the peak periods of incident waves and the modeled water depth. For the peak period of 14.08 s that resulted in the largest wavelength (305 m) among the examined input peak periods, the maximum water depth for the waves to feel the bottom is 152 m. This corresponded to x = 175 km (west side of the GS). Based on buoymeasured wave data offshore of the GS (e.g. NDBC 41002), the maximum offshore observed peak wave period that occurs once a while is 16 s. For this large peak period, the maximum water depth for waves to feel the bottom is 200 m, which corresponds to almost the west boundary of the GS. Therefore, it is expected that even for this large peak period, the wave profile would not change significantly because of current and bottom dissipation together. When input peak period was 11 s, wave height decreased as a result of bottom dissipation starting at x = 160 km and decreased consistently toward the coast (x = 0). The wave height decline for input peak period of 16 s started farther offshore in the vicinity of the G8 west border (x = 195 km). At x = 150 km, the difference between wave height resulting from the constant and variable depth models was attributed to active bottom dissipation in this coastal

280

300

260

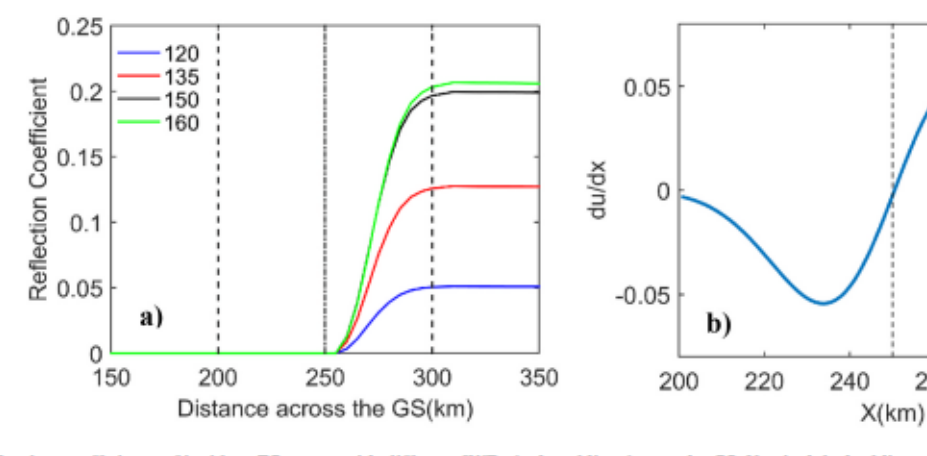


Fig. 7. a) Reflection coefficients of incident FC waves with different IWDs (colored lines) over the GS. Vertical dashed lines are GS west edge (x = 200 km), center (x = 250 km), and east edge (x = 300 km). b) The first derivative of the current with respect to distance across the GS, with GS center shown by vertical dashed line.

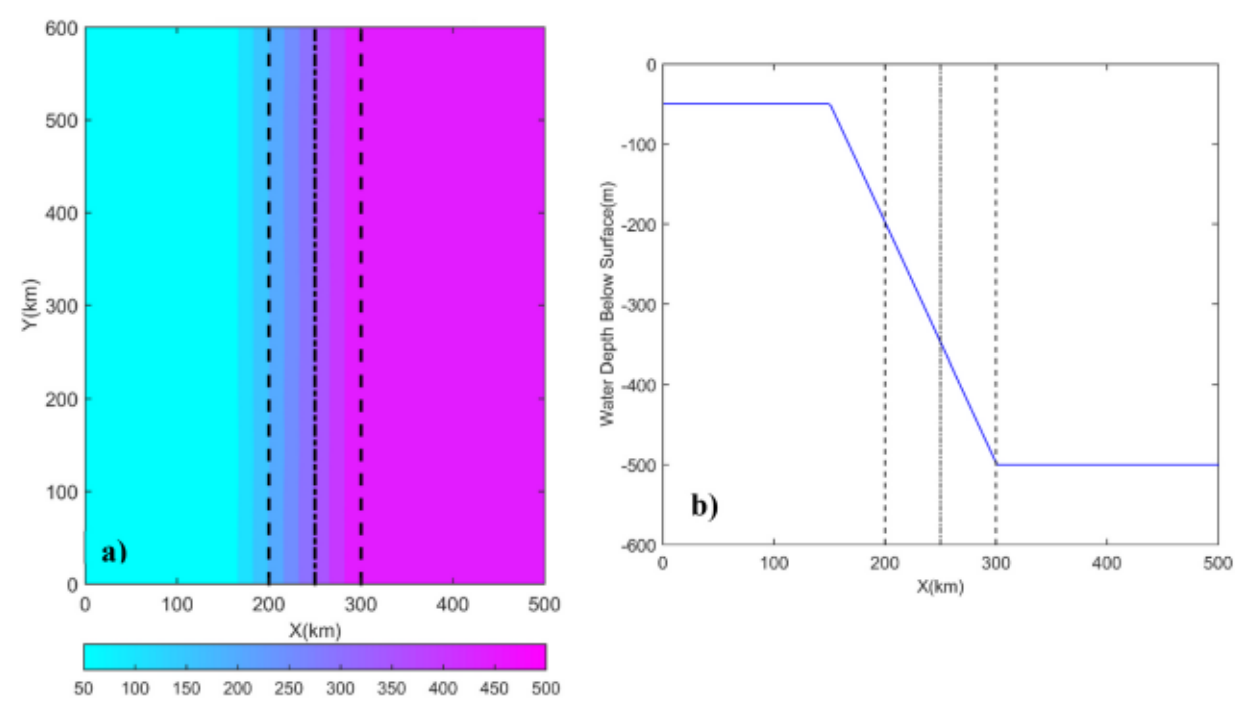
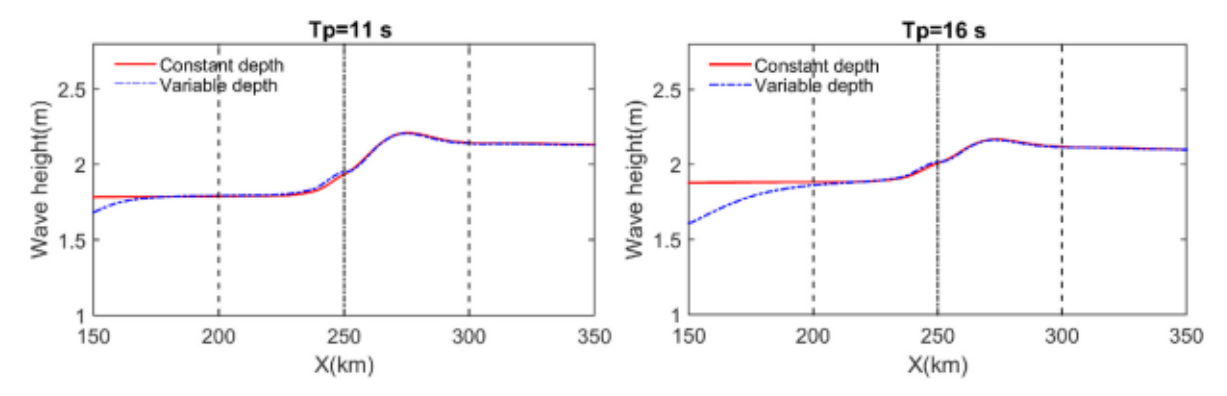


Fig. 8. a) Water depth variations (color shading, in meters) over the modeling area for the model with an idealized continental shelf. b) Water depth along a section parallel to the x-axis of (a). Dashed and solid lines indicate the borders and centerline of the GS.



Flg. 9. Variations of wave height across the GS for the scenarios with constant and variable depth and two peak periods (11 s, left, and 16 s, right) for input waves.

region.

These changes can also be explained by examining the frequency variations of the simulated bottom dissipation at different locations for two input wave periods (Fig. 10). Bottom dissipations were sampled at locations on the east, middle, and west of the GS as well as one coastal location about 100 km west of the GS. At deeper locations on the middle and east of the GS, the dissipation for both peak periods was several orders of magnitude smaller than those for the coastal and west locations, although dissipation was much larger for input peak period of 16 s. On the west side and coastal locations, results for both cases showed larger dissipation, consistent with their shallower depth. There the dissipation associated with peak period of 16 s was 1-2 orders of magnitude greater than that of 11 s. This greater dissipation contributed to more decline in wave height. Simulation results (not shown) with water depths shallower (100-150 m) than the actual GS depths demonstrated that frequency spectra over the G8 lose energy over their low-frequency lobe. In this case, the combined effect of the GS and shallow water worked like low- and high-pass filters on the frequency spectra. Although this result is not applicable for the GS over deeper water, it is relevant for other examples of intense ocean currents flowing over shallow depths.

4.2. Implications of current-induced wave modulation

As shown in the previous sections, propagation of waves over a current like the GS with a Gaussian-shaped transverse distribution can significantly modulate wave bulk and spectral properties across the current and its eastern and western regions. This modulation can have several implications on met-ocean processes and engineering applications associated with wave dynamics. In this section, two of these implications are discussed based on our model results.

4.2.1. Effect of modulation of waves by currents on surface drag and wave momentum flux

Wave effects on sea surface drag have been addressed by several studies (Taylor and Yelland, 2001; Drennan et al., 2003; Smith et al., 1992; Johnson et al., 1998), which aimed to provide a more accurate representation of the roughness length at the sea surface boundary layer using wave parameters. Use of the Charnock parameter, s_{ch} (Taylor and Yelland, 2001), is a traditional approach to quantify roughness length. The Charnock parameter uses inverse wave age c_p/u_{\bullet} where c_p is the wave celerity corresponding to peak frequency and u_{\bullet} is the wind

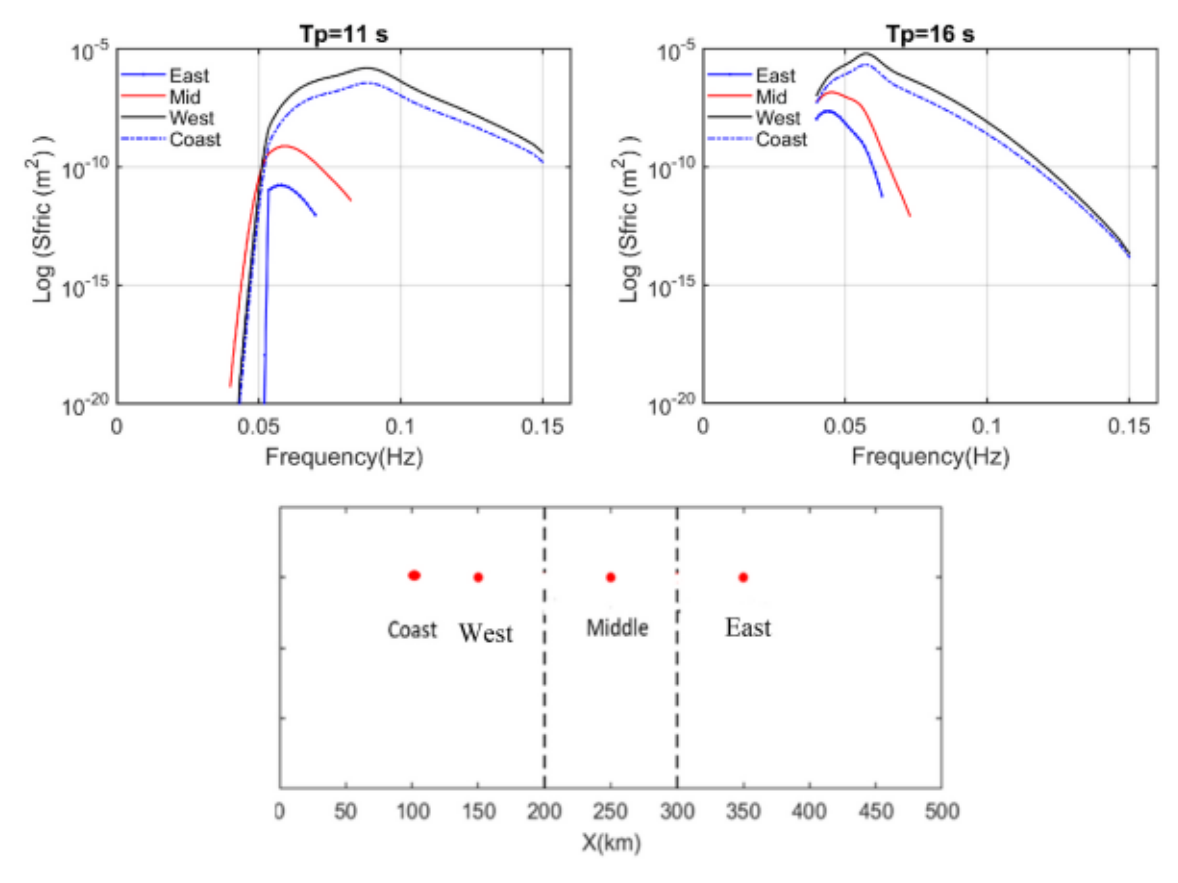


Fig. 10. Variations in bottom dissipation with frequency at four test points for two peak input wave periods (11 s, upper left, and 16 s, upper right). The lower panel specifies the locations of the test points over and near the GS.

friction velocity at the surface boundary layer (e.g., Smith et al., 1992; Johnson et al., 1998). Another approach to roughness length parameterization is using wave steepness, which may be combined with inverse wave age (Taylor and Yelland, 2001; Drennan et al., 2003). This approach has recently received more attention in coupled ocean-wave modeling (e.g. Warner et al., 2010; Zambon et al., 2014; Kim et al., 2018; Hegermiller et al., 2019). According to Taylor and Yelland (2001), wave-induced surface roughness length is calculated as:

$$Z_{e,w} = 1200H_s \left(\frac{H_s}{L_p}\right)^{4.5}$$
 (12)

where H_s is significant wave height and L_p is the wavelength corresponding to peak frequency. Recent studies also showed that not only the parametric wave properties such as height, length, and period affect surface drag, but energy distribution with frequency and direction do as well (Ting et al., 2012; Chalikov and Babanin, 2019). By using measurements of drag coefficient and wind speed within the sea surface boundary layer and analyzing the measured wave data in Lake George, Australia, Ting et al. (2012) implemented a numerical model of the sea surface boundary layer to study the dependence of the surface drag coefficient on wave directional spreading (DSPR). They found a significant correlation between DSPR and the drag coefficient that could cause up to 25% difference in estimation of the drag coefficient. In the work of Ting et al. (2012) and later in the detailed numerical simulation of the wind-wave boundary layer by Chalikov and Babanin (2019), the effect of wave spectral components on surface drag was calculated with the spectral distribution of the wave-induced momentum flux to the atmosphere as:

$$T_w(\omega, \theta) = kg\beta_{-k}(\tilde{\Omega}_k)S(\omega, \theta)$$
 (13)

where $T_w(\omega,\theta)$ is the 2-D spectrum of wave momentum flux, k is the wave number corresponding to each spectral component, g is the acceleration due to gravity in m s⁻², and $S(\omega,\theta)$ is the 2-D wave spectrum. Parameter β_{-k} $(\widetilde{\Omega}_k)$ is a non-dimensional function calculated using the wind speed at a height that is half of the wavelength for each spectral component. Application of the wave momentum spectra in estimating the surface drag coefficient has been demonstrated in several studies (Chalikov and Rainchik, 2011; Chalikov, 2018; Chalikov and Babanin, 2019), although due to the costly numerical implementation, it has not yet been considered as a practical option in coupled ocean modeling.

In our study, both the roughness length and wave momentum flux were affected by the GS over and near the current. Calculated roughness length (Eq. (12)) and simulation results for several IWDs (15°, 45°, 135°, and 150°) showed substantial variations across the GS and its offshore and coastal regions (Fig. 11a). The roughness lengths east of the GS center were larger than for the no-current case. The maximum roughness length occurred halfway between the middle and east edge of the G8 (x = 275 km) and was three-fold larger than the no-current value. The spatial variation pattern was very similar to that of wave height (Fig. 4) because the roughness length of Eq. (12) is a function of wave height. Roughness length dropped substantially below the no-current case for locations between the middle of the GS and the coast. Calculation of the total wave momentum flux using Eq. (13) and based on 2-D energy spectra from the simulation with the GS showed a similar pattern across the model domain (Fig. 11b). The total wave momentum fluxes were calculated by integrating the spectra of wave momentum flux (Eq. (13)) over the frequency-directional space. The momentum fluxes in Fig. 11b are presented for several wind speeds that account for the effect of local wind speed on momentum flux. The effect of wind speed was incorporated in the calculation of β_{-k} ($\tilde{\Omega}_k$), which is also a function of the angle difference between the wind and spectral components. Our

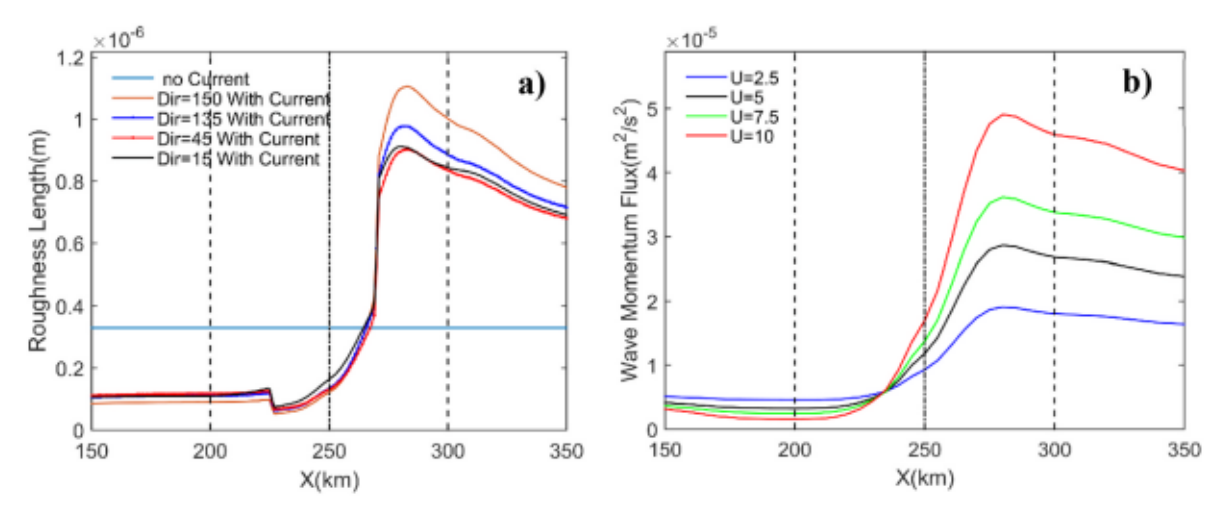


Fig. 11. a) Estimated surface roughness after the method of Taylor and Yelland (2001) across the model domain for four different incident wave directions compared to the no-current case. b) Variations of total wave-induced flux across the model for an incident wave from 150° under four local wind speeds U (m s⁻¹). Vertical dashed and solid lines indicate GS west, center, and east edges.

calculations assumed that the wind blew at a right angle to the incident wave (60° for wind direction and 150° for the incident wave). Wave momentum spectra on the west, center, and east of the GS (Fig. 12) show that directional coverage of momentum flux and its maximum decrease approaching the west side of the current, which is consistent with the total estimated flux in Fig. 11b. The peak value at the eastern location is attributable to the reflected part of the wave spectrum with large deviations from the assumed local wind direction. Although results shown here are for only one IWD (150°), results for other FC and CC directions confirmed that the GS substantially modulates parameters contributing to boundary layer dynamics in the presence of surface waves.

Modification of surface drag and wave momentum flux by currents can have important implications in predicting the intensity of a tropical cyclone (TC) when it passes over the GS. Based on the observational classification of swells under a tropical storm (Wright et al., 2001) and employing observational data of surface drag under a TC, Holthuijsen et al. (2012) suggested that surface roughness under a TC is azimuthally dependent and substantially increases under the TC's left front side due to the destructive effect of cross-swells on the oceanic spray foam layer in this region. These cross swells are associated with directional spreading of 45°-55° that also modulates the wave-atmosphere momentum flux. Interaction of TC-induced wave fields with a relatively wide WBC like the GS can produce more complicated spectral patterns (Hegermiller et al., 2019) with more spatial variations of directional spreading under the TC that can contribute to a more complex pattern of sea roughness spatial variation. The maximum potential intensity of TCs

is a function of the ratio between the enthalpy coefficient and sea drag (Emanuel, 1995; Bryan and Rotunno, 2009); therefore changes in the sea surface momentum flux and sea drag induced by the GS can affect TCs intensity prediction over the current.

4.2.2. Effect of modulation of waves by currents on wave energy resource assessment

Wave energy characterizations enable identification of hot spots of exploitable wave energy and inform design parameters for wave energy converters (WECs). Modeling studies have characterized wave energy for various ocean regions, including high-resolution modeling studies in U.S. waters (Ahn et al., 2021; Neary et al., 2020; Wu et al., 2020; Yang et al., 2017). However, most of these studies did not include the effect of background currents on wave characteristics, and thereby on energy-associated parameters. Although installing WEC facilities within regions of high-velocity currents like the GS and other WBCs may not be technically feasible, the effect of GS on wave energy parameters in offshore and coastal regions can nevertheless be assessed using results from this study.

To address the effect of a G8-like WBC on wave energy quantities, six International Electrotechnical Commission parameters (IEC, 2015; Allahdadi et al., 2019a) that are used as the basic parameters for quantifying wave energy were calculated using the spectral outputs from the simulations with and without currents (see appendix B for details on IEC parameters). The parameters include significant wave height (H₈), energy period (T_e), omni-directional wave power (J_{omni}), spectral width,

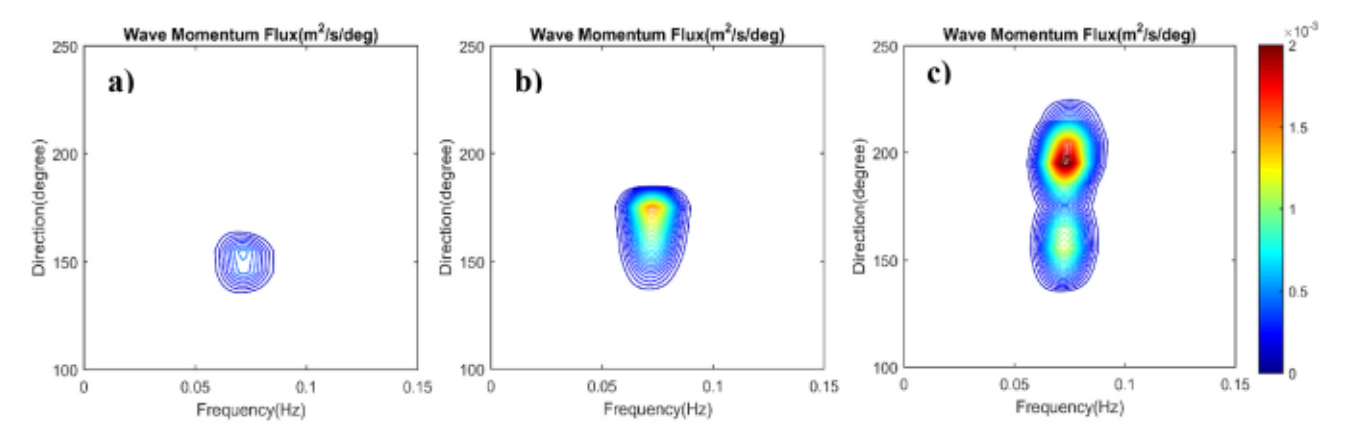


Fig. 12. Wave momentum flux spectra (color scale, in m²/s/deg) calculated using Eq. (13) from simulations with an incident wave at 150° at a) west side, b) center, and c) east side of the GS.

direction of maximum wave power, and directionality coefficient of maximum wave power. Each parameter has a specific implication in site selection and the short-term/long-term operation of WEC facilities. Calculations show that depending on the characteristics of the incident wave, variations of the parameters across the GS and its eastern and western regions can be significant (Table 2). The parameters were calculated using the spectral data obtained from simulations for incident waves with H_s 2 m and T_p 11 s and three IWDs (FC direction 135, CC direction 45, and through-current direction 90). For most IEC parameters, the FC case (135) resulted in the largest variations. It is most pronounced for H_s (18.18%), J_{omni} (36.36%), and the directionality coefficient (15.58%). For the CC case (45), variations for parameters are 3 12%. The smallest variations are mostly related to the through-current case (90). The six IEC parameters were also compared for an FC wave with IWD 150 to those from a no-current case (Fig. 13). Notable changes occur to the IEC parameters as a result of current modulation compared to the no-current case not only over the GS but also over the offshore and coastal regions. Thus modulation of waves by currents can significantly affect the accuracy of energy characterization, especially on the coastal side of the GS or any other WBC.

5. Summary and conclusions

Modulations of wave properties by ambient currents have been demonstrated through earlier observational, analytical, and numerical studies. Ocean currents can cause major spatial variabilities experienced by wave fronts within a broad spectrum of spatial scales. In the present study, we focused on the variations of swell properties induced by a Gulf Stream-like current. Compared to the study by Holthuijsen and Tolman (1991; herein HT91), which used 14 km spatial resolution, the present study resolved the GS-induced wave modulation at the much higher 1 km spatial resolution. As our analyses have shown, this higher resolution is crucial for resolving variations for regions with high spatial gradients of current speed. Our model setup utilized an idealized, fully 2D model

 $\begin{tabular}{ll} \textbf{Table 2} \\ Brief \ results \ of \ IEC \ parameters \ calculated \ using \ simulated \ wave \ spectra \ including the GS effect with H_s & 1.99 m, T_p & 11.1 s, and three wave directions. \\ Maximum \ and \ minimum \ values \ and \ percent \ variation \ across \ the \ model \ cross-section \ are \ given. \\ \end{tabular}$

SE (135)			
	Max.	Min.	Variations (%)
Hs(m)	2.2	1.8	18.18
Te(s)	10.4	10.2	1.96
Jomni(kw/m)	22.0	14	36.36
Spectral width	0.2202	0.2065	6.18
Dir Coefficient	0.89	0.77	15.58
ThetaMax(deg)	145	127	12.41
E (90)	· · · · · · · · · · · · · · · · · · ·	· · · · · · · · · · · · · · · · · · ·	
	Max.	Min.	Variations (%)
Hs(m)	2.05	1.98	3.4
Te(s)	10.30	10.06	2.3
Jomni(kw/m)	19.6	18.2	7.14
Spectral width	0.2143	0.2093	2.32
Dir Coefficient	0.972	0.971	0.10
ThetaMax(deg)	95	85	10.5
NE (45)		<u></u> -	
	Max.	Min.	Variations (%)
Hs(m)	2.09	1.90	9.10
Te(s)	10.30	10.0	3.0
Jomni(kw/m)	20.9	18.4	11.96
Spectral width	0.2155	0.2076	3.84
Dir Coefficient	0.97	0.92	5.15
ThetaMax(deg)	47	44	6.38

of the GS and offshore/coastal regions, with the GS flowing south to north and having a Gaussian current profile with a maximum current speed of 1.5 m s 1 . Swell parameters along the open (north, east, and south) boundaries were generally the same as in HT91, but more incident wave directions (IWDs) were examined for both following-current (FC) and counter-current (CC) cases. The much-higher spatial resolution of our model allowed us to discover several new and important details on modulation of waves by currents:

- 1. Our simulations showed that wave propagation over the GS from a FC direction such as 135 was associated with reflection from the current as a result of intense refraction of high-frequency wave components (or spectral components with large clockwise deviations from the IWD). This reflection took place on the east side and across the right half of the GS, causing a moderate to substantial increase in wave height (7 25%). This increase was not clearly detected in HT91 due to their low model resolution. This wave height amplification was different from the analytical quantification of the wave amplification factor across the GS that only considers the effects of refraction, straining, and radiation stress work. The wave profile resulting from the analytical solution was almost symmetrical relative to the GS centerline, since it did not include the asymmetrical wave reflection effect. One important alteration of wave height across the model domain caused by the GS was the substantial decrease of wave height west of the GS, where wave height dropped up to 80% depending on the IWD. This is an important finding that was not made in HT91since they only examined IWD which the wave height drop outside of the GS was less than 5%.
- 2. Variations of wave height across the GS for CC cases were consistent with analytical results, since both model and analytical solutions share common mechanisms contributing to wave height amplification. Our results showed that although refraction can strongly decrease wave height over the GS for CC cases, both straining and radiation stress work compensate for this reduction, so the resultant amplification factor is greater than 1 and wave height increases. In more direct counter-current cases (IWDs of 0 15), this wave amplification can be up to 33%. The GS rotated wave orthogonals clockwise and increased (decreased) DSPR for FC (CC) cases.
- 3. Both frequency and frequency-directional spectra across the model were affected by the GS. For the frequency spectra, CC case results agreed with analytical results for both spectral peak and peak frequency. The dominant straining effect increased the spectral peak of energy and decreased peak frequency in the center of the GS. The spectral energy peak decrease in the mid-GS for FC cases was also in agreement with analytical solutions, although reflection was also in play in addition to straining. For FC cases, the model and analytical results consistently showed slight increases of the peak frequency at this location. The 2D spectra for the CC cases showed additional components in the spectra at all locations across the model. The energy peak from these additional components was almost in the direction of current and accounted for spurious energy diffusion, which was filtered out in the calculation of wave parameters for all cases. Unlike the CC cases, the additional wave energy added to the spectrum for the FC cases at the locations on the eastern side and right half of the GS were realistic and accounted for the reflected energy over these regions. The reflection coefficients for each of the FC cases across the GS were calculated by separating and integrating this reflected energy portion. Reflection occurred only over the eastern half of the GS and the offshore regions outside of the GS with maximum reflection coefficients of $0.05 \, 0.2$ for IWDs of $120 \, - 160$.
- 4. With realistic ranges of water depth and maximum measured swell peak period in the GS region, bottom dissipation likely does not interact with current-modulated waves. Simulations with variable water depths showed that for a current flowing over water as shallow as 100 150 m, the simultaneous effect of current and bed dissipation

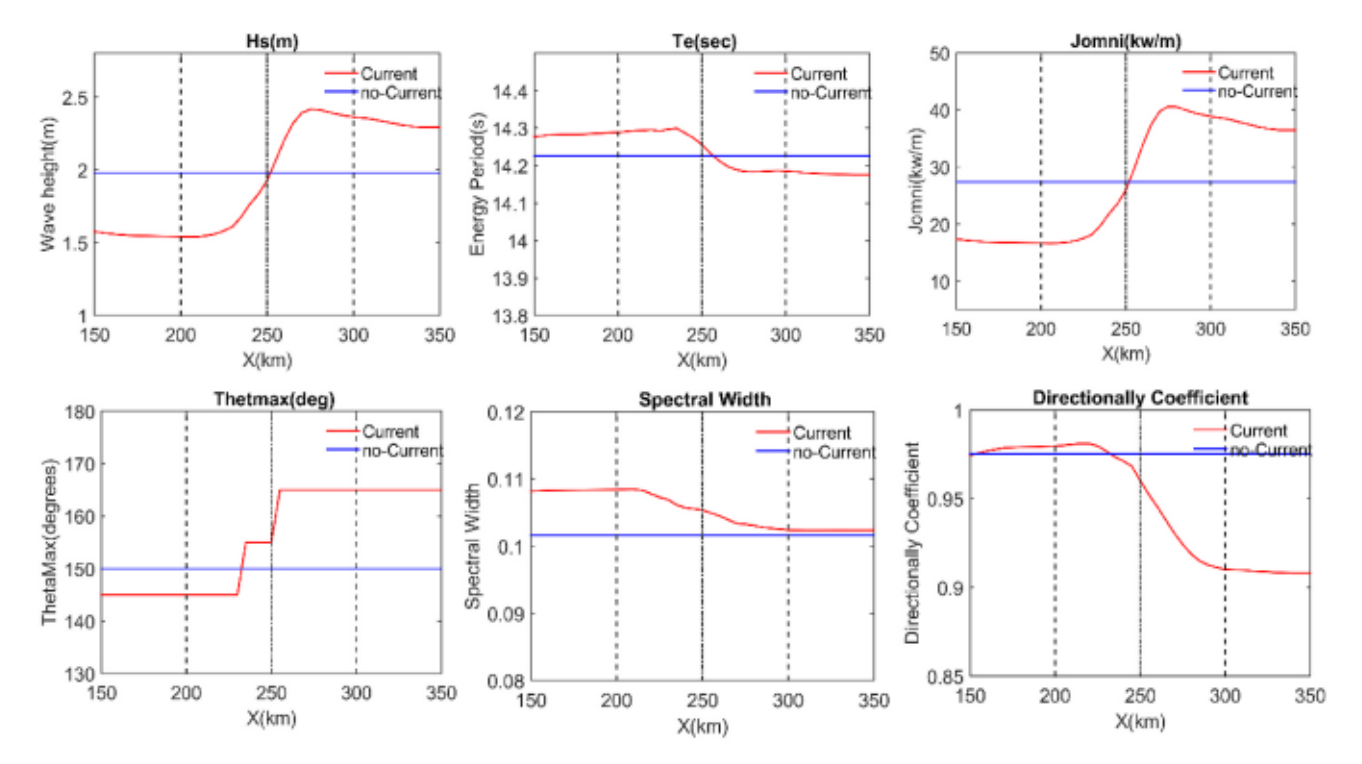


Fig. 13. Variations of six simulated IEC parameters across the GS and the eastern/western regions for an FC wave with IWD = 150° (red) in comparison with the calculated parameters for the no-current case (blue). Vertical dashed and solid lines are the west, center, and east edges of the GS.

can act as a combination of low- and high-pass filters on the frequency spectra.

Further analyses showed that GS modulation of swell parametric and spectral properties has several implications in ocean-atmosphere modeling and engineering. At the ocean-atmosphere boundary layer, waves play an important role in momentum exchange and in defining surface roughness. Simulated swell properties over the GS showed that modulation of swells by the current can increase the roughness length at the boundary layer three-fold. Including current-induced changes of swell properties can therefore improve the accuracy of dissipation quantification in wave models, which use spectral properties of swells to include the dissipation of wave profile caused by interaction with ocean turbulence.

One engineering application that can be strongly affected by G8 modulation of swells is wave energy characterization and assessment. The six IEC parameters used for locating energy hot spots and designing wave energy converters are altered moderately to significantly by the G8 depending on the characteristics of the still-water swells. For the case of swells from the southeast (IWD = 135°) with peak period of 11 s, the variations of omni-directional wave power from 50 km on the east side of the G8 to 50 km down-wave (offshore and coastal regions and the G8 area) was as large as 36%. The variations of other IEC parameters were as high as 18%. Considering these significant variations and the expense and effort of generating high-resolution wave model hindcasts to support accurate wave energy resource characterization and assessment studies (e.g. Allahdadi et al., 2019a and Allahdadi et al., 2021 for the U. S. East Coast and Gulf of Mexico), the present study demonstrates the importance of including currents in these wave hindcast models.

The present study investigates how an idealized GS modulates properties of waves that propagate through it. No wind and the related generation source terms were included in this study to simplify processes. In reality, winds moving in the opposite direction of the GS may produce waves that are trapped inside the current, leading to locally increased wave height over the current. Improved understanding of this process will be reported in a future correspondence.

Availability Statement

All results used in the analyses presented in this paper are obtained either from simulations using SWAN or calculations based on the analytical formula. The simulation details, model setups, and all the analytical formulations are presented and discussed in the paper in detail. Therefore, the results can be reproduced by following these instructions.

Declaration of competing interest

The authors declare that they have no known competing financial interests or personal relationships that could have appeared to influence the work reported in this paper.

Data availability

No data was used for the research described in the article.

Acknowledgments

We appreciate funding support from NSF grants OCE-1559178271 and OCE-1851421, NOAA grant NA16NOS0120028, Sandia National Laboratories grant 1994475, North Carolina Renewable Ocean Energy Program, USGS/Marine Hazards and Resources Program, and by Congressional appropriations through the Additional Supplemental Appropriations for Disaster Relief Act of 2019 (H.R. 2157). Sandia National Laboratories is a multi-mission laboratory managed and operated by National Technology and Engineering Solutions of Sandia, LLC, a wholly owned subsidiary of Honeywell International, Inc., for the US Department of Energy's National Nuclear Security Administration under contract DE-NA0003525. This paper describes objective technical results and analyses. Any subjective views or opinions that might be expressed in the paper do not necessarily represent the views of the U.S. Department of Energy or the United States Government. We thank Jennifer Warrillow for her editorial assistance.

Appendix A

Definitions of terms used herein, as they apply to the idealized Gulf Stream along the east coast of the U.S. in this paper (Fig. 2).

Following-current (FC) wave: An incident wave that has a component in the direction of the current. FC directions include incident waves between 90 to 180 relative to model north.

Counter-current (CC) wave: An incident wave that has a component that opposes the current. CC directions include incident waves between 0 and 90 relative to model north.

Western border of the GS: The border of the Gulf Stream facing the coast. In the model configuration and results presented herein, the western border of the Gulf Stream corresponds to x 200 km.

Eastern border of the GS: The border of the Gulf Stream facing the offshore region. In the model configuration and results presented herein, the eastern border of the Gulf Stream corresponds to x 300 km.

Middle of the GS: The location exhibiting the largest Gulf Stream current speed. In the model configuration and results presented herein, the middle of the Gulf Stream corresponds to x 250 km.

Upstream: In the model configuration in this paper, upstream of each location represents a location with a smaller Y coordinate.

Downstream: In the model configuration in this paper, downstream of each location represents a location with a larger Y coordinate.

Appendix B

Based on the International Electrotechnical Commission (IEC) 2015 standards, the following six parameters derived from the frequency-directional wave spectra are required for evaluation of the wave energy resources and design of wave energy converter (WEC) facilities:

Significant wave height H_s 4 m_0

Energy period $T_e = \frac{m_{-1}}{m_0}$

Omni-directional wave power $J = g c_g i S_{ij} f_{i}$

Spectral width $_0$ $\frac{m_0m_{-2}}{m_{-1}^2}$ 1

Direction of maximum wave power Jmax

Directionality coefficient of maximum wave power $d = \frac{J_{Jmax}}{T}$

where m_n is the nth-order spectral moment, is water density, g is the acceleration due to gravity, c_g is the wave group velocity, S_{ij} is spectral energy corresponding to a spectral component with ith frequency and jth direction, and f_i and g are spectral resolutions.

References

- Ahn, S., Neary, V.S., Allahdadi, M.N., He, R., 2021. Nearshore wave energy resource characterization along the East Coast of the United States. Renew. Energy 172, 1212 1224. https://doi.org/10.1016/j.renene.2021.03.037.
- Allahdadi, M.N., Gunawan, B., Lai, J., He, R., Neary, V.S., 2019a. Development and validation of a regional-scale high-resolution unstructured model for wave energy resource characterization along the US East Coast. Renew. Energy 136, 500 511. https://doi.org/10.1016/j.renene.2019.01.020.
- Allahdadi, M.N., He, R., Neary, V.S., 2019b. Predicting ocean waves along the US east coast during energetic winter storms: sensitivity to whitecapping parameterizations. Ocean Sci. J. 15, 691 715. https://doi.org/10.5194/os-15-691-2019.
- Allahdadi, M.N., He, R., Ahn, S., Chartrand, C., Neary, V.S., 2021. Development and calibration of a high-resolution model for the Gulf of Mexico, Puerto Rico, and the U. S. Virgin Islands: implication for wave energy resource characterization. Ocean Eng. 235, 109304 https://doi.org/10.1016/j.oceaneng.2021.109304.
- Ardhuin, F., Gille, S.T., Menemenlis, D., Rocha, C.B., Rascle, N., Chapron, B., Gula, J., Molemaker, J., 2017. Small-scale open ocean currents have large effects on wind wave heights. J. Geophys. Res.: Oceans 122, 4500 4517. https://doi.org/10.1002/2016.10012413.
- Barnes, M.A., Rautenbach, C., 2020. Toward operational wave-current interactions over the Agulhas current system. J. Geophys. Res.: Oceans 125, e2020JC016321. https:// doi.org/10.1029/2020JC016321.
- Baschek, B., 2005. Wave-current interaction in tidal fronts. In: Aha Hulikoa Hawaiian Winter Workshop 2005, pp. 131–138.
- Berline, L., Testut, C.-E., Brasseur, P., Verron, J., 2006. Variability of the Gulf Stream position and transport between 1992 and 1999: a re-analysis based on a data assimilation experiment. Int. J. Rem. Sens. 27, 417 432. https://doi.org/10.1080/ 01431160500254882
- Bretherton, F.P., Garrett, C.J.R., Lighthill, M.J., 1968. Wave trains in inhomogeneous moving media. Proc. Roy. Soc. Lond. Math. Phys. Sci. 302, 529 554. https://doi.org. 10.1098/rspa.1968.0034.
- Bryan, G.H., Rotunno, R., 2009. Evaluation of an analytical model for the maximum intensity of tropical cyclones. J. Atmos. Sci. 66, 3042–3060. https://doi.org/ 10.1175/2009.JAS3038.1.
- Beya, I., Buckham, B., Robertson, B., 2021. Impact of tidal currents and model fidelity on wave energy resource assessments. Renew. Energy 176, 50 66. https://doi.org/ 10.1016/j.renene.2021.05.039.
- Chalikov, D., Rainchik, S., 2011. Coupled numerical modelling of wind and waves and the theory of the wave boundary layer. Boundary-Layer Meteorol. 138, 1–41. https://doi.org/10.1007/s10546-010-9543-7.

- Chalikov, D., 2018. Numerical modeling of surface wave development under the action of wind. Ocean Sci. 14, 453 470. https://doi.org/10.5194/os-14-453-2018.
- Chalikov, D., Babanin, A.V., 2019. Parameterization of wave boundary layer. Atmos 10, 686. https://doi.org/10.3390/atmos10110686.
- Dean, R.G., Dalrymple, R.A., 1991. Water Wave Mechanics for Engineers and Scientists. World Scientific, Singapore.
- Dobson, E.B., Irvine, D.E., 1983. Investigation of Gulf Stream Ring Detection with Spaceborne Altimeter Using Mean Sea Height, Wave Height and Radar Cross Section. Appl. Phys. Lab., Johns Hopkins Univ., Laurel, Md.. Rep. JHU/APL SIR3U-005, 51 pp., Space Dep.
- Drennan, W.M., Graber, H.C., Hauser, D., Quentin, C., 2003. On the wave age dependence of wind stress over pure wind seas. J. Geophys. Res.: Oceans 108. https://doi.org/10.1029/2000JC000715.
- Emanuel, K.A., 1995. Sensitivity of tropical cyclones to surface exchange coefficients and a revised steady state model incorporating eye dynamics. J. Atmos. Sci. 52, 3969 3976. https://doi.org/10.1175/1520-0469.
- Gangopadhyay, A., Chaudhuri, A.H., Taylor, A.H., 2016. On the nature of temporal variability of the Gulf Stream Path from 75 to 55 W. Earth Interact. 20 (9), 17.
- Hasselmann, K., Barnett, T.P., Bouws, E., Carlson, H., Cartwright, D.E., Enke, K., Ewing, J.A., Gienapp, H., Hasselmann, D.E., Kruseman, P., Meerburg, A., Müller, P., Olbers, D.J., Richter, K., Sell, W., Walden, H., 1973. Measurements of wind wave growth and swell decay during the joint North Sea wave project (JONSWAP). Dtsch. Hydrogr. Z. Suppl. 12, A8.
- Hedges, T.S., 1980. Some effects of currents on wave spectra. In: 1st Indian Conference on Ocean Engineering at. IIT Madras.
- Hegermiller, C.A., Warner, J.C., Olabarrieta, M., Sherwood, C.R., 2019. Wave current interaction between Hurricane Matthew wave fields and the Gulf Stream. J. Phys. Oceanogr. 49, 2883 2900. https://doi.org/10.1175/JPO-D-19-0124.1.
- Holthuijsen, L.H., Tolman, H.L., 1991. Effects of the Gulf Stream on ocean waves.

 J. Geophys. Res.: Oceans 96, 12755 12771. https://doi.org/10.1029/91JC00901.
- Holthuijsen, L.H., Powell, M.D., Pietrzak, J.D., 2012. Wind and waves in extreme hurricanes. J. Geophys. Res.: Oceans 117. https://doi.org/10.1029/2012JC007983.
- Hopkins, J., Elgar, S., Raubenheimer, B., 2016. Observations and model simulations of wave-current interaction on the inner shelf. J. Geophys. Res.: Oceans 121, 198 208. https://doi.org/10.1002/2015JC010788.
- IEC, 2015. Marine Energy Wave, Tidal and Other Water Current Converters
 Wave Energy Resource Assessment and Characterization. International
 Electrotechnical Commission, Geneva, Switzerland.
- Johnson, J.W., 1947. The refraction of surface waves by currents. Eos, Transactions American Geophysical Union 28, 867–874. https://doi.org/10.1029/ TR028i006p00867.

- Johnson, H.K., H jstrup, J., Vested, H.J., Larsen, S.E., 1998. On the dependence of sea surface roughness on wind waves. J. Phys. Oceanogr. 28, 1702 1716. https://doi. org/10.1175/1520-0485(1998)028 1702:OTDOSS 2.0.CO;2.
- Kim, T., Moon, J.-H., Kang, K., 2018. Uncertainty and sensitivity of wave-induced sea surface roughness parameterisations for a coupled numerical weather prediction model. Tellus Dyn. Meteorol. Oceanogr. 70, 1 18. https://doi.org/10.1080/ 16000870.2018.1521242.
- Lavaud, L., Bertin, X., Martins, K., Arnaud, G., Bouin, M.-N., 2020. The contribution of short-wave breaking to storm surges: the case Klaus in the Southern Bay of Biscay. Ocean Model. 156, 101710 https://doi.org/10.1016/j.ocemod.2020.101710.
- Liu, P.L.-F., Cho, Y.-S., Kostense, J.K., Dingemans, M.W., 1992. Propagation and trapping of obliquely incident wave groups over a trench with currents. Appl. Ocean Res. 14, 201–213.
- Liu, A.K., Jackson, F.C., Walsh, E.J., Peng, C.Y., 1989. A case study of wave-current interaction near an oceanic front. J. Geophys. Res.: Oceans 94, 16189 16200. https://doi.org/10.1029/JC094iC11p16189.
- Lucas, C., Guedes Soares, C., 2015. On the modelling of swell spectra. Ocean Eng. 108, 749 759. https://doi.org/10.1016/j.oceaneng.2015.08.017.
- Meadows, G.A., Shuchman, R.A., Tseng, Y.C., Kasischke, E.S., 1983. SEASAT synthetic aperture radar observations of wave-current and wave-topographic interactions. J. Geophys. Res.: Oceans 88, 4393 4406. https://doi.org/10.1029/
- McKee, W.D., 1975. A two turning-point problem in fluid mechanics. Math. Proc. Camb. Phil. Soc. 77, 581 590. https://doi.org/10.1017/S0305004100051409.
- McKee, W.D., 1977. The reflection of water waves by shear currents. PAGE 115, 937 949. https://doi.org/10.1007/BF00881217.
- McLeish, W., Ross, D.B., 1985. Wave refraction in an ocean front. J. Geophys. Res.: Oceans 90, 11929 11938. https://doi.org/10.1029/JC090iC06p11929.
- Misra, V., 2020. Chapter 4 the intra-Americas seas. In: Misra, V. (Ed.), Regionalizing Global Climate Variations. Elsevier, pp. 71 113. https://doi.org/10.1016/B978-0-12-821826-6 00004-7
- Moreira, R.M., Peregrine, D.H., 2012. Nonlinear interactions between deep-water waves and currents. J. Fluid Mech. 691, 1–25. https://doi.org/10.1017/ifm.2011.436.
- Neary, V.S., Ahn, S., Seng, B.E., Allahdadi, M.N., Wang, T., Yang, Z., He, R., 2020. Characterization of extreme wave conditions for wave energy converter design and project risk assessment. J. Mar. Sci. Eng. 8, 289. https://doi.org/10.3390/ jmse8040289.
- Neu, W.L., Won, Y.S., 1990. Propagation schemes for wind wave models with finite depth and current. In: Rahman, M. (Ed.), Proceedings 11th International Annual Conference of the Canadian Applied Mathematics Society, Ocean Wave Mechanics, Computational Fluid Dynamics and Mathematical Modelling. Computational Mechanics, Boston, Mass., pp. 947–954
- Onorato, M., Residori, S., Bortolozzo, U., Montina, A., Arecchi, F.T., 2013. Rogue waves and their generating mechanisms in different physical contexts. Physics Reports, Rogue waves and their generating mechanisms in different physical contexts 528, 47 89. https://doi.org/10.1016/j.physrep.2013.03.001.
- Peregrine, D.H., 1976. Interaction of water waves and currents. In: Yih, C.-S. (Ed.), Advances in Applied Mechanics. Elsevier, pp. 9 117. https://doi.org/10.1016/ S0065-2156(08)70087-5.
- Ponce de León, S., Guedes Soares, C., 2021. Numerical modelling of the effects of the Gulf Stream on the wave characteristics. J. Mar. Sci. Eng. 9, 42. https://doi.org/10.3390/ imse9010042.
- Prakash, K.R., Pant, V., 2020. On the wave-current interaction during the passage of a tropical cyclone in the Bay of Bengal. Deep sea research Part II: topical studies in oceanography. Atmosphere-Ocean Dynamics of Bay of Bengal - 2 172, 104658. https://doi.org/10.1016/j.dsr2.2019.104658.
- Romero, L., Lenain, L., Melville, W.K., 2017. Observations of surface wave current interaction. J. Phys. Oceanogr. 47, 615 632. https://doi.org/10.1175/JPO-D-16-0108.1.

- Rusu, L., Bernardino, M., Guedes Soares, C., 2011. Modelling the influence of currents on wave propagation at the entrance of the Tagus estuary. Ocean Eng. 38, 1174–1183. https://doi.org/10.1016/j.oceaneng.2011.05.016.
- Shyu, J.-H., Tung, C.-C., 1999. Reflection of oblique waves by currents: analytical solutions and their application to numerical computations. J. Fluid Mech. 396, 143 182. https://doi.org/10.1017/S0022112099006126.
- Smith, S.D., Anderson, R.J., Oost, W.A., Kraan, C., Maat, N., De Cosmo, J., Katsaros, K.B., Davidson, K.L., Bumke, K., Hasse, L., Chadwick, H.M., 1992. Sea surface wind stress and drag coefficients: the hexos results. Boundary-Layer Meteorol. 60, 109 142. https://doi.org/10.1007/BF00122064.
- SWAN, 2015. User Manual, Cycle III Version 41.01A. Delft University of Technology, Delft, the Netherlands.
- Tamura, H., Waseda, T., Miyazawa, Y., Komatsu, K., 2008. Current-induced modulation of the ocean wave spectrum and the role of nonlinear energy transfer. J. Phys. Oceanogr. 38, 2662 2684. https://doi.org/10.1175/2008JPO4000.1.
- Taylor, P.K., Yelland, M.J., 2001. The dependence of sea surface roughness on the height and steepness of the waves. J. Phys. Oceanogr. 31, 572 590. https://doi.org/ 10.1175/1520-0485(2001)031 0572:TDOSSR 2.0.CO:2.
- Ting, C.-H., Babanin, A.V., Chalikov, D., Hsu, T.-W., 2012. Dependence of drag coefficient on the directional spreading of ocean waves. J. Geophys. Res: Oceans 117. https://doi.org/10.1029/2012JC007920.
- Toffoli, A., Waseda, T., Houtani, H., Cavaleri, L., Greaves, D., Onorato, M., 2015. Rogue waves in opposing currents: an experimental study on deterministic and stochastic wave trains. J. Fluid Mech. 769, 277 297. https://doi.org/10.1017/jfm.2015.132.
- Tolman, H.L., 1990. The influence of unsteady depths and currents of tides on wind-wave propagation in shelf seas. J. Phys. Oceanogr. 20, 1166 1174. https://doi.org/10.1175/1520-0485(1990)020 1166:TIOUDA 2.0.CO;2.
- Warner, J., Armstrong, B., He, R., Zambon, J., 2010. Development of a coupled ocean-Atmosphere-Wave-Sediment transport (COAWST) modeling system. Ocean Model. 35 (3), 230 244. https://doi.org/10.1016/j.ocemod.2010.07.010.
- Wright, C.W., Walsh, E.J., Vandemark, D., Krabill, W.B., Garcia, A.W., Houston, S.H., Powell, M.D., Black, P.G., Marks, F.D., 2001. Hurricane directional wave spectrum spatial variation in the open ocean. J. Phys. Oceanogr. 31, 2472 2488. https://doi.org/10.1175/1520-0485(2001)031 2472:HDWSSV 2.0.CO;2.
- Wu, W.-C., Wang, T., Yang, Z., García-Medina, G., 2020. Development and validation of a high-resolution regional wave hindcast model for U.S. West Coast wave resource characterization. Renew. Energy 152, 736–753. https://doi.org/10.1016/j. renene_2020.01.077.
- Yang, Z., Neary, V.S., Wang, T., Gunawan, B., Dallman, A.R., Wu, W.-C., 2017. A wave model test bed study for wave energy resource characterization. Renew. Energy, Wave and Tidal Resource Characterization 114, 132 144. https://doi.org/10.1016/ i.renene.2016.12.057.
- Zambon, J.B., He, R., Warner, J.C., 2014. Investigation of Hurricane ivan using the coupled ocean-Atmosphere-Wave-Sediment transport (COAWST) model. Ocean Dynam. 64 (11), 1535–1554. https://doi.org/10.1007/s10236-014-0777-7.
- Zeng, X., He, R., 2016. Gulf Stream variability and a triggering mechanism of its large meander in the South Atlantic Bight. J. Geophys. Res.: Oceans 121, 8021–8038. https://doi.org/10.1002/2016JC012077.
- Zieger, S., Babanin, A.V., Erick Rogers, W., Young, I.R., 2015. Observation-based source terms in the third-generation wave model WAVEWATCH. Ocean Model, Waves and coastal, regional and global processes 96, 2 25. https://doi.org/10.1016/j. ocemod.2015.07.014.
- Zijlema, M., 2009. Parallel, unstructured mesh implementation for swan. In: Coastal Engineering 2008. World Scientific Publishing Company, pp. 470 482. https://doi. org/10.1142/9789814277426_0040.
- Zijlema, M., 2010. Computation of wind-wave spectra in coastal waters with SWAN on unstructured grids. Coast Eng. 57, 267 277. https://doi.org/10.1016/j. coastaleng.2009.10.011.